

Ⓞ Mechanisms of Low-Level Jet Formation in the U.S. Mid-Atlantic Offshore

EMILY DE JONG^{Ⓞ, a}, ELIOT QUON,^b AND SHASHANK YELLAPANTULA^b

^a *California Institute of Technology, Pasadena, California*

^b *National Renewable Energy Laboratory, Golden, Colorado*

(Manuscript received 24 April 2023, in final form 19 October 2023, accepted 3 November 2023)

ABSTRACT: Low-level jets (LLJs), in which the wind speed attains a local maximum at low altitudes, have been found to occur in the U.S. mid-Atlantic offshore, a region of active wind energy deployment as of 2023. In contrast to widely studied regions such as the U.S. southern Great Plains and the California coastline, the mechanisms that underlie LLJs in the U.S. mid-Atlantic are poorly understood. This work analyzes floating lidar data from buoys deployed in the New York Bight to understand the characteristics and causes of coastal LLJs in the region. Application of the Hilbert–Huang transform, a frequency analysis technique, to LLJ case studies reveals that mid-Atlantic jets frequently occur during times of adjustment in synoptic-scale motions, such as large-scale temperature and pressure gradients or frontal passages, and that they do not coincide with motions at the native inertial oscillation frequency. Subsequent analysis with theoretical models of inertial oscillation and thermal winds further reveals that these jets can form in the stationary geostrophic wind profile from horizontal temperature gradients alone—in contrast to canonical LLJs, which arise from low-level inertial motions. Here, inertial oscillation can further modulate the intensity and altitude of the wind speed maximum. Statistical evidence indicates that these oscillations arise from stable stratification and the associated frictional decoupling due to warmer air flowing over a cold sea surface during the springtime land–sea breeze. These results improve our conceptual understanding of mid-Atlantic jets and may be used to better predict low-level wind speed maxima.

SIGNIFICANCE STATEMENT: The purpose of this work is to identify and characterize the atmospheric mechanisms that result in an occasional low-level maximum in the wind speed off the U.S. mid-Atlantic coastline. Our findings show that these low-level jets form due to horizontal temperature gradients arising from fronts and synoptic systems, as well as from the land–sea breeze that forces warmer air over the cold ocean surface. This work aids predictability of such jets, improves our understanding of this coastal environment, and has implications for future deployment of offshore wind energy in this region.

KEYWORDS: Jets; Marine boundary layer; Coastal meteorology; Spectral analysis/models/distribution

1. Introduction

Low-level jets (LLJs) broadly describe local maxima in wind speed that occur near the surface, as opposed to more typical monotonically increasing winds with altitude. These LLJ wind phenomena have important effects on pollutant transport and air quality (Ryan et al. 1998; Delgado et al. 2015), as well as enhancing moisture transport associated with deep convection and strong precipitation (Maddox 1983; Zhang and Fritsch 1986; Higgins et al. 1997). More recently, as interest in wind energy technology has risen, so has interest in the characteristics and atmospheric mechanisms of LLJs in wind-rich resource areas such as the southern Great Plains (SGP) (e.g., Gutierrez et al. 2017; Wimbhurst and Greene 2019; Gadde and Stevens 2021a) and the California coast (Optis et al. 2020). The U.S. mid-Atlantic recently joined the list as the focal point of national incentives to develop offshore wind energy on the East Coast (White House 2021; Shields et al. 2022; U.S. Environmental Protection Agency

2023). LLJs have also been found to occur in this offshore region near New Jersey and Long Island (Colle and Novak 2010; Debnath et al. 2021), but relatively little attention has been paid to these New York (NY) Bight jets compared with their more canonical counterparts in the SGP and California coast. This work analyzes recent floating lidar data from buoys deployed in the NY Bight to disentangle the effects of potential LLJ mechanisms.

The canonical Blackadar mechanism (Blackadar 1957) of inertial oscillation (IO) describes jets in the SGP, which occur at night with a regular diurnal cycle in the summertime. (Many definitions of the LLJ, in fact, presuppose this mechanism and nocturnal nature; however, this work defines an LLJ by its maximum in wind speed alone.) In the Blackadar conceptual model, the onset of atmospheric stability at nighttime initiates a deviation of the instantaneous winds from a steady-state wind that balances horizontal pressure gradients and shear stresses (Cuxart and Jiménez 2007). This deviation leads to rotation of the wind vector about its equilibrium at the Coriolis frequency, which can induce a local maximum in the wind speed with respect to altitude (Parish et al. 1988; Van de Wiel et al. 2010; Shapiro and Fedorovich 2010; Du and Rotunno 2014; Carroll et al. 2019). This model of LLJ formation has also been shown to apply to nocturnally recurrent jets at Cabauw in the Netherlands (Baas et al. 2009), over the

Ⓞ Denotes content that is immediately available upon publication as open access.

Corresponding author: Emily de Jong, edejong@caltech.edu

DOI: 10.1175/JAS-D-23-0079.1

© 2023 American Meteorological Society. This published article is licensed under the terms of the default AMS reuse license. For information regarding reuse of this content and general copyright information, consult the AMS Copyright Policy (www.ametsoc.org/PUBSReuseLicenses).

Brought to you by NATL RENEWABLE ENERGY LAB | Unauthenticated | Downloaded 01/26/24 06:11 PM UTC

Weddell Sea (Andreas et al. 2000), and over the Baltic coast (Högström and Smedman-Högström 1984; Smedman et al. 1993, 1995). A key feature of these nocturnal jets is frictional decoupling that occurs between the boundary layer and flows at higher altitudes due to nighttime onset of stability over the daytime-warmed land surface (Du and Rotunno 2014, e.g.), which is not expected to be as pronounced in an offshore environment with approximately constant sea surface temperatures over diurnal time scales. However, Smedman et al. (1995) found that the land–sea temperature contrast during daytime was crucial for development of an LLJ in the Baltic Sea, suggesting that the flow of warm continental air over the sea surface could induce frictional decoupling.

In contrast, coastal jets in California have been linked to a baroclinic mechanism, in which winds remain in geostrophic balance and a wind speed maximum forms due to the coupling of the thermal wind balance with a surface layer below (Parish 2000). This mechanism has also been shown to enhance IO-triggered LLJs in areas of sloped terrain, such as the SGP (Holton 1967; Shapiro and Fedorovich 2009; Parish and Oolman 2010). Related to these horizontal temperature gradients, coastal jets in California have also been linked to the land–sea breeze (LSB) (Zemba and Friehe 1987; Douglas 1995; Burk and Thompson 1996; Holt 1996; Sgouros and Helmis 2009). Topography and terrain have likewise been shown to contribute to California coastal jets through the shape of the coastline (Beardsley et al. 1987; Burk and Thompson 1996) and to be the dominant factor in barrier jets that form along mountain ranges, such as the Sierra Nevada (Parish 1982) and the Antarctic shelf (Parish 1983). Finally, LLJs in many regions have been linked to frontal passage (Ostdiek and Blumen 1995, 1997; Lundquist 2003; Kalashnik 2004; Sgouros and Helmis 2009), which could represent a particular case of the baroclinic forcing mechanism.

While LLJs in the U.S. mid-Atlantic have been studied for decades, the scientific community has not yet yielded a clear consensus on their causes. Observational studies of LLJs on the East Coast have focused on nocturnal inversion (Doyle and Warner 1991) and stable stratification induced by LSBs (Helmis et al. 2013; Debnath et al. 2021) as sources of frictional decoupling and IO, as well as on contributions of mountainous topography to formation of jets (Doyle and Warner 1991; Rabenhorst et al. 2014). McCabe and Freedman (2023) recently linked LLJs in the NY Bight to land–sea breezes, citing the contribution of differential heating and the land–sea temperature difference. Other studies utilizing weather forecasting models have revealed contributions to LLJs from large-scale gradients in temperature and pressure, the slope of the Appalachian topography, frontal passages, and diurnal land–sea temperature contrasts (Zhang et al. 2006; Colle and Novak 2010; Rabenhorst et al. 2014; Aird et al. 2022). Recent modeling studies of the mid-Atlantic offshore region suggest a strong seasonality in both LLJs (Aird et al. 2022) and sea-breeze events (Xia et al. 2022), which further suggests that temperature and pressure gradients contribute to jets in this coastal environment.

The present work examines floating lidar buoy data from the NY Bight to disentangle mechanisms that may contribute

to these gradients at different time scales, including synoptic-scale flow, frontal passages, and diurnal land–sea temperature contrasts. While many existing studies of LLJs only consider local effects in order to isolate the low-level maxima from large-scale phenomena such as frontal passages, we make no such distinction, preferring instead to characterize any and all low-level maxima in the wind speeds. First, we consider statistics based on 2 years of data in the region to understand the relationship of LLJ activity with frontal events, seasonality, and local factors such as the air–sea temperature difference. Next, we generalize the Hilbert–Huang transform (HHT) analysis of Lundquist (2003) to examine frequency ranges suggested by the data, considering different physical processes rather than a single presupposed mechanism such as IO. We further investigate inertial motions and synoptic signatures found from this frequency analysis through a conceptual framework of IO and thermal wind balance (as in Ostdiek and Blumen 1997). Section 2 of this paper describes the dataset and these analysis techniques, including the HHT and conceptual models. Section 3 then presents the results described above, beginning with the 2-yr statistics, followed by frequency analysis, and concluding with conceptual models. Finally, section 4 summarizes the primary findings and offers additional insights for future work.

2. Methods and data

a. Lidar and buoy data

Wind data used in this study come from two floating lidar buoys in the NY Bight funded by the New York State Energy Research and Development Authority (NYSERDA) (NYSERDA 2022). The buoys are located at (39°58′09.40″N, 72°43′00.09″W) for buoy E05 North and (39°32′48.38″N, 73°25′44.01″W) for buoy E06 South (hereafter referred to as E05 and E06) (see Fig. A1 in appendix A for a graphical depiction of the buoy location), supplying lidar wind measurements at 10-min frequency every 20 m above mean sea level up to 200 m, as well as meteorological data measured at the buoy. The limited vertical extent of the lidar data restricts analysis to very low-level jets and cannot identify jets with a maximum above 180-m altitude (the final measurement altitude of 200 m is required to show a decrease in wind speed above this 180-m level). Unlike other nearby studies (Zhang et al. 2006; Colle and Novak 2010; Rabenhorst et al. 2014), this limitation may reduce detection of LLJs resulting from inertial oscillation that would result in maxima near or above the boundary layer height, compared with contributions from land–sea breeze and frontal passages which are visible in near-surface winds. The buoys are separated by approximately 47 km north–south and 60 km east–west, for a distance of 77 km.

The available data included a single 2-yr period of concurrent measurements at both buoys spanning September 2019–September 2021 which we use for statistical analysis of coinciding factors with LLJs in the region. Later analyses are restricted to buoy E06 in the springtime of April–June 2020 and several 6-day case studies within this time window due to improved data availability over E05 during this time period. Additional data quality control is applied in computing jet statistics: lidar

readings reporting a wind speed measurement greater than 70 m s^{-1} at any altitude or with measurements at fewer than 3 out of the 10 lidar reading altitudes are considered invalid, as no validation of the lidars was performed for results beyond these thresholds (NYSERDA 2022).

The HHT frequency analysis additionally uses Doppler lidar data from the Atmospheric Radiation Measurement (ARM) SGP site C1 over a 12-day period from 9 to 20 June 2018 (Newsom and Krishnamurthy 2023). This dataset extends up to 4.3 km in altitude, but analysis is restricted to the lowest 24 levels (as in Bodini et al. 2021), reaching an altitude of 688 m, which sufficiently captures most nocturnal LLJs. This 688-m altitude is additionally a reasonable upper bound of the boundary layer height in the SGP (Bodini et al. 2021), and thus presents a useful analog to the 200-m maximum altitude of the NY Bight lidar data and typically lower height of the marine boundary layer.

LLJs are identified in all lidar datasets according to the criteria of Debnath et al. (2021). These criteria are season agnostic and intended to identify low-level maxima in the winds, which may be relevant to wind energy: 1) the 150-m (reference turbine hub height) wind speed exceeds the cut-in speed of 3 m s^{-1} ; 2) the wind profile displays a local maximum within the measured altitude levels; and 3) the drop in wind speed above the local maximum exceeds 1.5 m s^{-1} or 10% of the maximum wind speed, whichever is higher.

b. Surface analysis

Discussion of fronts and pressure systems are based on interpretation of surface analysis maps from the National Weather Service Weather Prediction Center (WPC). Statistical results presented in this work also include statistics related to the frequency of frontal passage in the region. The 3-h WPC CONUS surface analysis maps are obtained for the 2-yr period corresponding to available lidar data from September 2019–September 2021. Images are analyzed for the presence of a front (warm, cold, or occluded) within a 100-km radius of buoy E06, as illustrated in Fig. A1. This radius is determined from multiplying a characteristic wind speed of 10 m s^{-1} by the interval between surface analysis frames (3 h). A front is determined to coincide with an LLJ event if the front is present in the frame within 3 h of a sustained LLJ event. A sustained LLJ event is defined as a time period in which there is no more than a 1-h gap in consecutive lidar measurements (every 10 min) displaying an LLJ. Statistics are reported as a fraction of 10-min time intervals which belong to an extended jet event out of all times, and out of times in which a front is also present. Significance of the difference between these two fractions is reported as the p value from the binomial test.

c. Temperature gradients computed from WRF

Model data

To approximate horizontal temperature gradients for LLJ case studies, this study uses archived data for corresponding case dates from a multiyear Weather Research and Forecasting (WRF) Model run over the U.S. mid-Atlantic region (Bodini et al. 2020). The archived data include hourly output

of temperature fields up to 260-m altitude. Gradients are approximated using the difference in temperature at coordinates that are $\pm 0.2^\circ$ latitude and longitude from buoy E06 (or approximately $\pm 22 \text{ km}$), averaged in altitude up to 200 m and in time for the case date of interest. The magnitude of temperature gradients computed this way is not sensitive to increasing the horizontal distance used in differencing, provided the points used in the computation are both over the ocean.

d. Hilbert–Huang transform

The HHT is applied to velocity components from the lidar data according to the procedure of Lundquist (2003). In brief, the time-varying velocity component (U or V) at a single altitude level is decomposed into its intrinsic mode functions (IMFs). The Hilbert transform is applied to each IMF to recover a complex signal: $A(t)\exp[i\theta(t)]$ (where i is the unit imaginary number). This resulting signal can be understood as a sine wave with amplitude $A(t)$ and phase $\theta(t)$ both varying in time, and the local-in-time frequency of the sine wave can be derived by differentiating $\theta(t)$. Both the decomposition into IMFs and the Hilbert transform are computed using the Python package Empirical Mode Decomposition (EMD) (Quinn et al. 2021).

Frequencies and amplitudes resulting from the HHT are then analyzed in two ways. First, we generate a frequency spectra, where the frequencies of a given IMF are weighted by their associated amplitude and aggregated in time to generate histograms of the normalized “power” associated with various frequency ranges (Fig. 7). This weighting and aggregation is performed within the EMD package. Second, a time–height mapping of the Hilbert amplitudes filtered for particular frequency ranges and summed over all IMFs is presented (in Figs. 8–11). This second analysis is similar to that of Helmis et al. (2015), but the filtered frequency ranges are much broader, inclusive over the range 1×10^{-6} to $5 \times 10^{-5} \text{ Hz}$ (corresponding to periods of 12 days to 6 h), and centered about peaks in the frequency power spectra, rather than specific inertial or diurnal frequencies.

e. Theoretical models

The latter half of the analysis fits time- and height-varying lidar velocity data from the three mid-Atlantic LLJ case studies (as in Figs. 9–11) to analytical models of IO and thermal wind balance following the procedures of Ostdiek and Blumen (1997). For an IO, data are fit to the equations

$$\begin{aligned} u(z, t) &= u_{ss}(z) + A(z)\sin[ft + \phi(z)] \\ v(z, t) &= v_{ss}(z) + A(z)\cos[ft + \phi(z)]. \end{aligned} \quad (1)$$

The parameters $u_{ss}(z)$, $v_{ss}(z)$, $A(z)$, and $\phi(z)$ (with a value at each lidar altitude z) are varied to minimize the mean squared error between the fits $u(z, t)$ and the time series data.

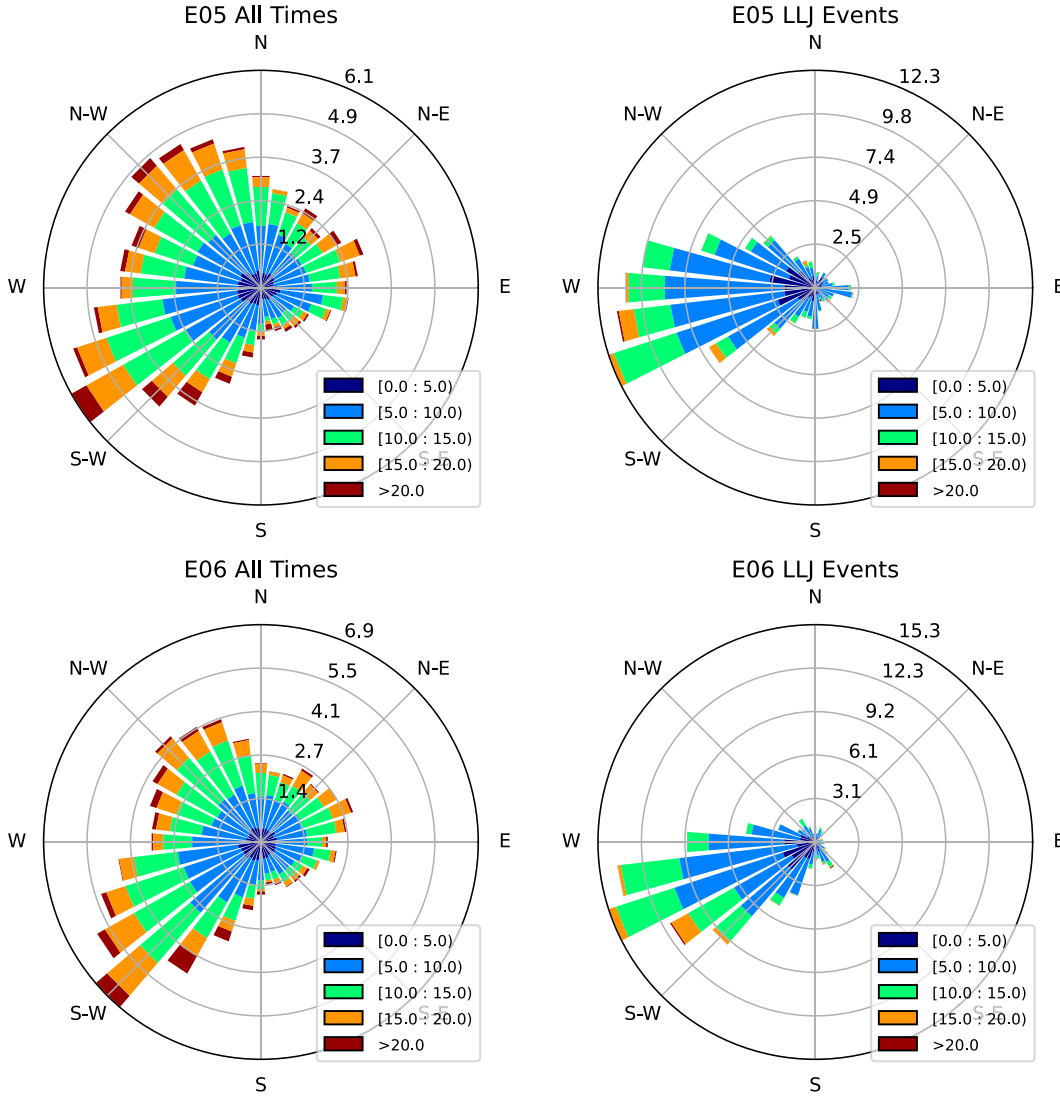


FIG. 1. Frequency of wind speed and direction at $z = 160$ m for buoys (top) E05 and (bottom) E06, (left) for all times and (right) for LLJ events only. Bar height corresponds to the frequency of occurrence of the wind direction as a percentage of data, and coloring of the bar is proportional to the number of data points in various wind speed bins (see legend; units: m s^{-1}).

Later, we explore the steady-state velocity profiles through the lens of thermal wind balance, as an Ekman layer coupled to a surface layer. The Ekman layer solution is given by

$$\begin{aligned} u_{\text{ss}}(z) &= (u_{g0} + u_{gz}z) + e^{-\eta}[(u_0 - u_{g0})\cos\eta + (v_0 - v_{g0})\sin\eta], \\ v_{\text{ss}}(z) &= (v_{g0} + v_{gz}z) + e^{-\eta}[(v_0 - v_{g0})\cos\eta - (u_0 - u_{g0})\sin\eta], \end{aligned} \quad (2)$$

where $\eta = z/H$, H being the Ekman layer depth, and (u_{g0}, v_{g0}) are the geostrophic wind components at the surface. The surface winds u_0 and v_0 are derived to satisfy a surface layer matching condition:

$$\frac{\partial(u, v)}{\partial z} = \frac{A}{H}(u, v), \quad (3)$$

which implies

$$\begin{aligned} u_0 &= \frac{(2 + A)u_{g0} + (1 + A)Hu_{gz} - (Av_{g0} - Hv_{gz})}{1 + (1 + A)^2}, \\ v_0 &= \frac{(2 + A)v_{g0} + (1 + A)Hv_{gz} + (Av_{g0} - Hv_{gz})}{1 + (1 + A)^2}. \end{aligned} \quad (4)$$

In Eq. (4), (u_{gz}, v_{gz}) refer to the vertical gradients of the geostrophic wind components, which can be related to horizontal temperature differences through thermal wind balance. Parameters of this model are varied to minimize the mean squared error across altitudes between the steady-state profiles $u_{\text{ss}}(z)$ and $v_{\text{ss}}(z)$ found in Eq. (1) and the predicted Ekman layer solution. In a freely varying version of

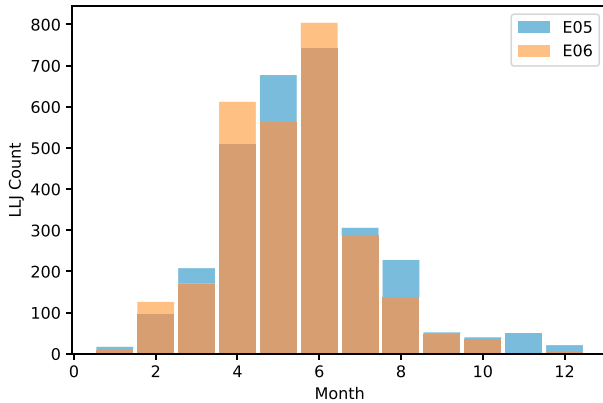


FIG. 2. Count of LLJ occurrences by month of the year for both NYSERDA buoys (colors).

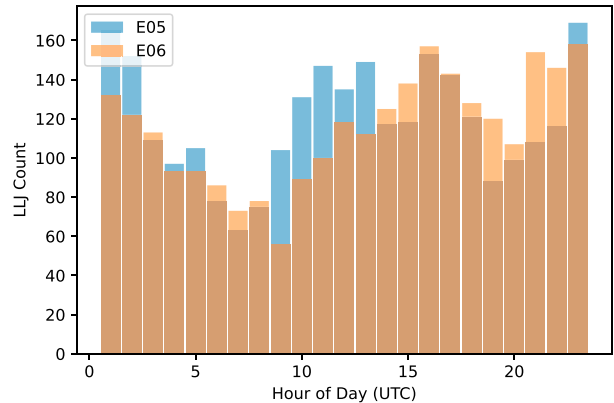


FIG. 3. Count of LLJ occurrences by hour of the day for both NYSERDA buoys (colors).

the optimization, the parameters u_{g0} , v_{g0} , v_{gz} , v_{gz} , H , and A are allowed to vary, with u_{gz} and v_{gz} constrained to fall within $(-0.1, 0.1) \text{ s}^{-1}$, A within $(0, 10)$, and H within $(0, 400) \text{ m}$ to ensure physical solutions. In a second, semi-constrained version of this optimization, the parameters u_{gz} and v_{gz} are approximated from horizontal temperature gradients computed from WRF data over the same time period as the IO fit. These gradients are then fixed, and only u_{g0} , v_{g0} , H , and A vary in the optimization.

3. Results and discussion

a. Statistical indicators of low-level jets in the New York Bight

Analysis of the lidar-measured wind speeds at both NYSERDA buoys over a 2-yr period (spanning September 2019–September 2021) reveals LLJs that are detected in 2.9% and 3.5% of valid lidar readings collected at buoys E05 and E06, respectively. These frequencies likely underestimate the presence of wind speed maxima in the boundary layer due to the limited 200-m vertical extent of the lidar data. Buoy E06 reports data over 78% of the 2-yr time period, with two large gaps in available data spanning September 2020–January 2021 and August 2021–December 2021. Buoy E05 reports data over 97% of the 2-yr period and experiences intermittent gaps in data up to 12 h in duration during June and October 2020. Based on this data availability, we focus on statistics for buoy E05, while later selecting case studies from spring 2020 from buoy E06.

Winds in the region are predominantly southwesterly at both buoys (Fig. 1), with the strongest winds arising from a southwesterly along-coast direction. Restricting this analysis to only the LLJ events, however, reveals that LLJs have a much stronger correlation with west-southwesterly wind direction compared with all data at each buoy. The LLJ distribution favors moderate wind speeds and few occasions where the wind speed exceeds 18 m s^{-1} . These findings are consistent with the results of Debnath et al. (2021), who found that high-shear periods at the same NYSERDA buoy sites typically occur during southwesterly flows with a bias toward west-southwest. Jets are slightly more westerly than the

overall data, and this enhanced cross-coast direction could imply influence of the LSB.

In agreement with previous work (e.g., Debnath et al. 2021; Aird et al. 2022; Colle and Novak 2010; McCabe and Freedman 2023), we find that LLJs occur most frequently in the spring months of April–June (Fig. 2) and in afternoon and evening hours local time (Fig. 3), with a second peak in frequency in the late morning. LLJs are much less frequent in the autumnal and early winter months of September–January, though this finding may be impacted by missing data in the case of E06. In contrast to nocturnal SGP LLJs, which typically occur after sunset, LLJs occur least frequently in the nighttime hours (0400–1000 UTC). This key difference indicates that the primary driving mechanism of mid-Atlantic LLJs is unlikely to be IOs triggered by nocturnal stability. However, diurnal cycles in the land–sea temperature gradient may nevertheless be important to controlling the formation and timing of LLJs (Colle and Novak 2010; McCabe and Freedman 2023). For instance, the cross-coast land–sea temperature gradient could directly strengthen along-coast winds during a jet event through thermal wind balance. The findings of McCabe and Freedman (2023) that LLJs frequently coincide with LSBs, which peak in the late afternoon hours, additionally implicate a role of the local air–sea temperature difference.

Consistent with the dominant wind direction, jets are more likely to occur when the pressure gradient between the two buoys (Fig. 4, left), which follows an approximately along-coast southwesterly direction, is positive. Pressure differences greater than 1 hPa between the buoys are less likely to be found during an LLJ event, which agrees with the finding that LLJs are less likely to exhibit 150-m wind speeds exceeding 15 m s^{-1} (Fig. 1). However, LLJ events are more likely to exhibit positive horizontal temperature gradients (higher temperatures to the southwest) of all magnitudes (Fig. 4, right). These findings further implicate a thermal wind effect: horizontal temperature gradients, potentially related to the LSB, drive the vertical structure of the geostrophic wind, which may play an important role in the formation of jets in the region. Furthermore, Fig. 5 indicates that jet events are much

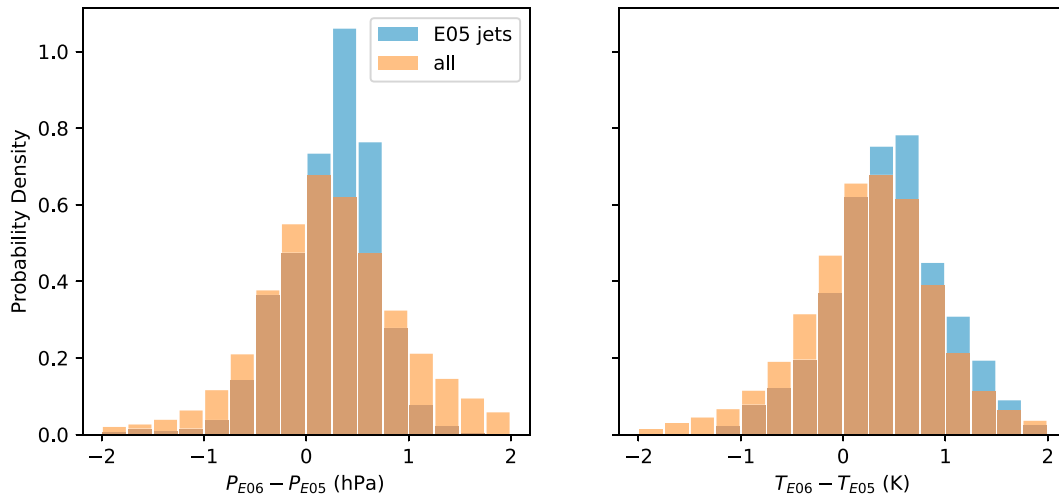


FIG. 4. Probability density of horizontal differences in (left) pressure and (right) temperature measured at the two NYSEERDA buoys (southwest minus northeast buoy) for LLJ events and all data points.

more likely than average to exhibit a positive air–sea temperature difference. This feature is consistent with the finding that LLJs predominantly occur in the springtime and the afternoon. It further suggests that jets may be associated with a more stable atmosphere, leading to a frictional decoupling that triggers an IO, as in [Smedman et al. \(1995\)](#). The springtime prevalence of jets further suggests an association with a land–sea breeze pushing warmer air over a colder sea surface as found in [McCabe and Freedman \(2023\)](#), and the enhanced presence of LLJs during daytime compared with nighttime ([Fig. 3](#)) further supports LSBs as a contributing factor through horizontal temperature gradients and/or induced stability.

Fronts, which have been linked to LLJs in several studies (e.g., [Mori 1990](#); [Ostdiek and Blumen 1997](#); [Sgouros and Helmis 2009](#); [Helmis et al. 2013](#); [Carroll et al. 2019](#)), are an extreme case of horizontal temperature gradients, and may

contribute to the role of thermal winds in LLJ formation. Comparison of LLJ events with the WPC Surface Analysis archive reveals an enhanced probability of an LLJ event occurring during a time of frontal activity, compared with the baseline frequency. Using the criteria described in [section 2](#) to identify jet events, we find that 6.9% of time points at buoy E05 are associated with an LLJ event; when a front is present, the frequency of LLJ-associated time points rises to 12.0%, representing a 5% increase in likelihood of LLJs in the presence of a front ($p < 0.001$). This increase in jet activity with frontal passage was especially prominent in the springtime months of 2020, with an increase of 10% probability over the baseline of 14.9% LLJ-associated times in April–June 2020 ($p < 0.001$). Thus, LLJs in all seasons showed an enhanced probability of occurring in temporal proximity to a front in the region. This finding builds on observations of southwesterly

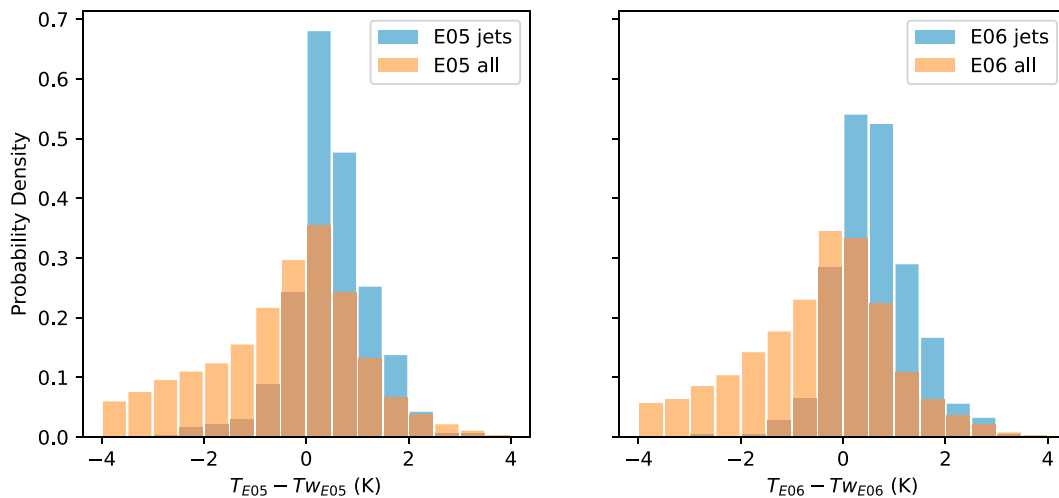


FIG. 5. Probability of air–sea temperature $T - T_w$ difference measured at each NYSEERDA buoy [(left) E05, (right) E06], for LLJ events and for all data points.

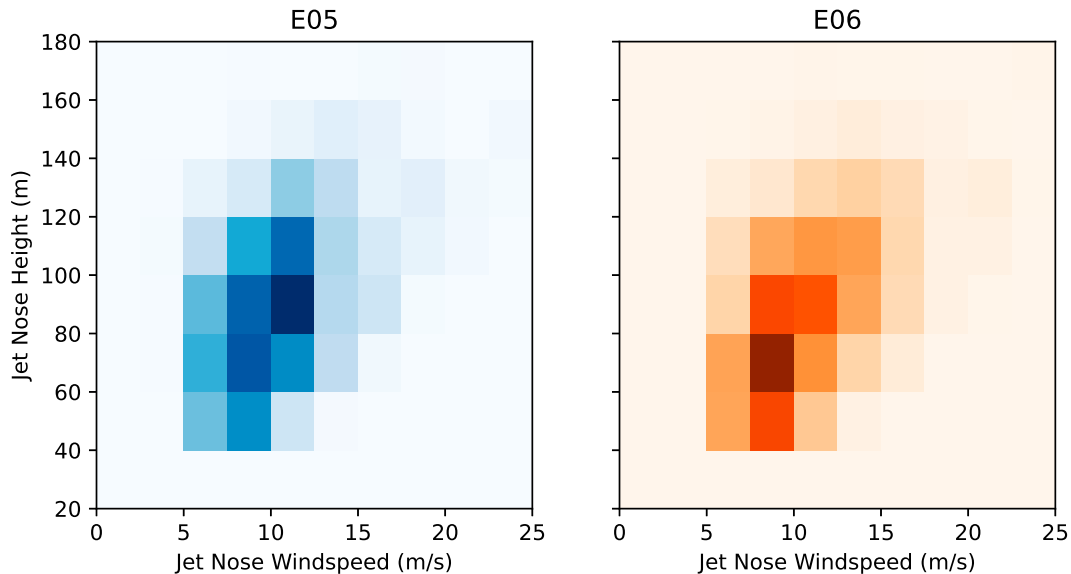


FIG. 6. Joint distribution of jet-nose heights and jet-nose wind speeds for all LLJ events from the two NYSERDA buoys over a 2-yr period from September 2019 to September 2021.

gradients (Fig. 4) to indicate a likely role of temperature and pressure gradients in creating LLJs in the region. Notably, however, the prevalence of LLJs during times of frontal activities is significantly lower than the 2/3 rate of occurrence of LLJs during LSBs found by McCabe and Freedman (2023), which suggests that the discontinuities associated with a front are less conducive to LLJs than the milder gradients associated with the LSB.

Jets at the NYSERDA buoys most frequently exhibit a jet-nose maximum wind speed of around 10 m s^{-1} at an altitude of 60–80 m (Fig. 6). These very low-level events contrast the land-based measurements of (Zhang et al. 2006), who found jets over Fort Meade, Maryland, with maximum wind speeds concentrated at a 400 m altitude and higher. Our finding likely reflects the limited vertical extent of the lidar data, which only reaches a 200-m altitude, as well as the difference in jet characteristics over land versus over the sea. Nevertheless, these near-surface jets in the NY Bight warrant interest, as they present wind speed maxima, and therefore negative vertical shear, at altitudes that would fall within the rotor layer of offshore wind turbines. These jets occur with speeds at or above the turbine rated wind speed, for which a turbine produces maximum power [see, e.g., the International Energy Agency’s 15-MW offshore reference wind turbine described in Gaertner et al. (2020)].

b. Frequency analysis

To distinguish mid-Atlantic LLJs from the background frequency characteristics of the region, we consider three 6-day periods at buoy E06, which contain sustained or repeated LLJ events of 6 h or more, as well as the entire 3-month 2020 springtime period containing these events. (The same periods at buoy E05 show similar frequency spectra but with worse data availability over the 2020 springtime.) In addition, we

use as reference a 12-day period from the ARM SGP site with regular recurring LLJs [previously studied for wind-plant applications in Bodini et al. (2021)] in order to compare the NY Bight jets against those with a well characterized Blackadar mechanism. Figure 7 displays the amplitude-weighted HHT frequencies at a single altitude near the typical jet-nose height aggregated over time for these five datasets. We note that for a given dataset, the peaks in each wind component typically correspond to the same characteristic frequencies, but the relative amplitude or power varies between wind components. This trend corroborates coupling between zonal (U) and meridional (V) winds as expected while indicating that directional factors, such as horizontal gradients, may impact the winds asymmetrically. The patterns seen in Fig. 7 are repeated at different altitudes in the data (not shown) with consistency in the dominant frequencies and variability in relative weighting of each IMF, particularly near the surface.

The SGP dataset in Fig. 7 (top row) displays strong peaks in the frequency spectra at 26 h, which is near the diurnal period, and at 19 h, which corresponds to the inertial period at this latitude. Lower-frequency peaks (134, 63 h) can be interpreted to correspond to synoptic time scales and mechanisms, whereas higher-frequency peaks are attributable to mesoscale phenomena, such as cloud and precipitation events (Lundquist 2003). Turbulence and other microscale frequencies have been excluded from the analysis due to their low normalized power in the HHT spectra. The HHT spectra of the full 2020 springtime period in the mid-Atlantic (Fig. 7, second row) shows strong separation of the time scales associated with each IMF, from the mesoscale periods of IMF’s 1–4, to a subinertial period of 14 h associated with IMF 5, a near-diurnal period of IMF 6, and larger synoptic periods for IMF 7 and greater. Four characteristic frequency ranges corresponding to these peaks in the SGP data and the full

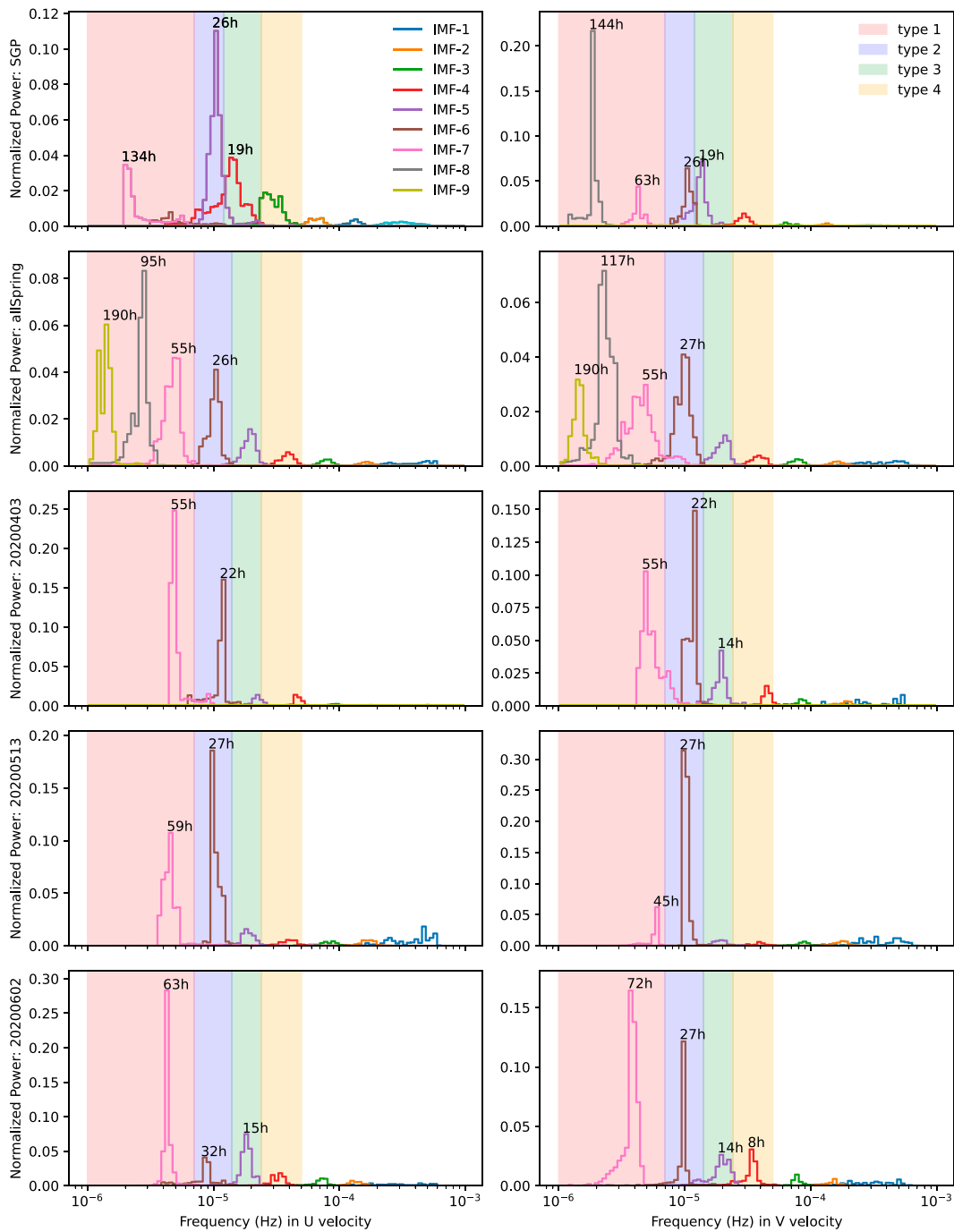


FIG. 7. Amplitude-weighted Hilbert–Huang transform frequency spectra in (left) U and (right) V velocities for five datasets for each intrinsic mode of the signal. Rows show data (from top to bottom) at the ARM SGP site C1, 403 m above ground level: a 12-day period beginning on 9 Jun 2018; at NYSERDA buoy E06, 160 m above mean sea level: 91 days spanning April–June 2020; and 6-day periods at NYSERDA buoy E06 beginning 2 Jun, 13 Mar, and 3 Apr 2020. Peaks with a normalized power above 0.02 are labeled with the period (units: h) corresponding to the frequency of that peak. Shadings denote the frequency ranges listed in Table 1.

springtime NYSERDA data are identified in Table 1 for further investigation and are shaded in Fig. 7. The two intermediate frequency ranges (types 2 and 3) are separated by the location of overlap of IMFs 5 and 6.

While previous works have used the HHT to specifically filter for inertial frequencies to identify evidence of IO (Lundquist 2003; Helmis et al. 2013), the spectra in Fig. 7 do not support the presence of an 18–19-h period in the mid-

TABLE 1. Frequency ranges investigated in Figs. 8–11 and the characteristic period about which the range is centered, selected based on results presented in Fig. 7. Note that frequency types are labeled from lowest to highest frequency—opposite from the IMF numbering, which tends to go from highest to lowest frequency.

Cases	Type 1	Type 2	Type 3	Type 4
NYSERDA buoy E06	1.0×10^{-6} to 7.0×10^{-6} Hz (60 h)	7×10^{-6} to 1.4×10^{-5} Hz (26 h)	1.4×10^{-5} to 2.4×10^{-5} Hz (14 h)	2.4×10^{-5} to 5×10^{-5} Hz (8 h)
ARM SGP C1	1.0×10^{-6} to 7.0×10^{-6} Hz (60+ h)	7×10^{-6} to 1.2×10^{-5} Hz (26 h)	1.2×10^{-5} to 2.4×10^{-5} Hz (19 h)	2.4×10^{-5} to 5×10^{-5} Hz (8 h)

Atlantic, unlike in the SGP. The spectra do, however, show a peak for a period of 22 h (in the case of 3 April 2020) to 27 h (13 May and 2 June 2020), as well as a peak at 14 h in the full springtime dataset and some velocity components of the case

dates. For the SGP data, frequency ranges 2 and 3 are cleanly categorized as diurnal and inertial, respectively, whereas the NYSERDA data better support a frequency range that encompasses both characteristic periods: a near-diurnal frequency

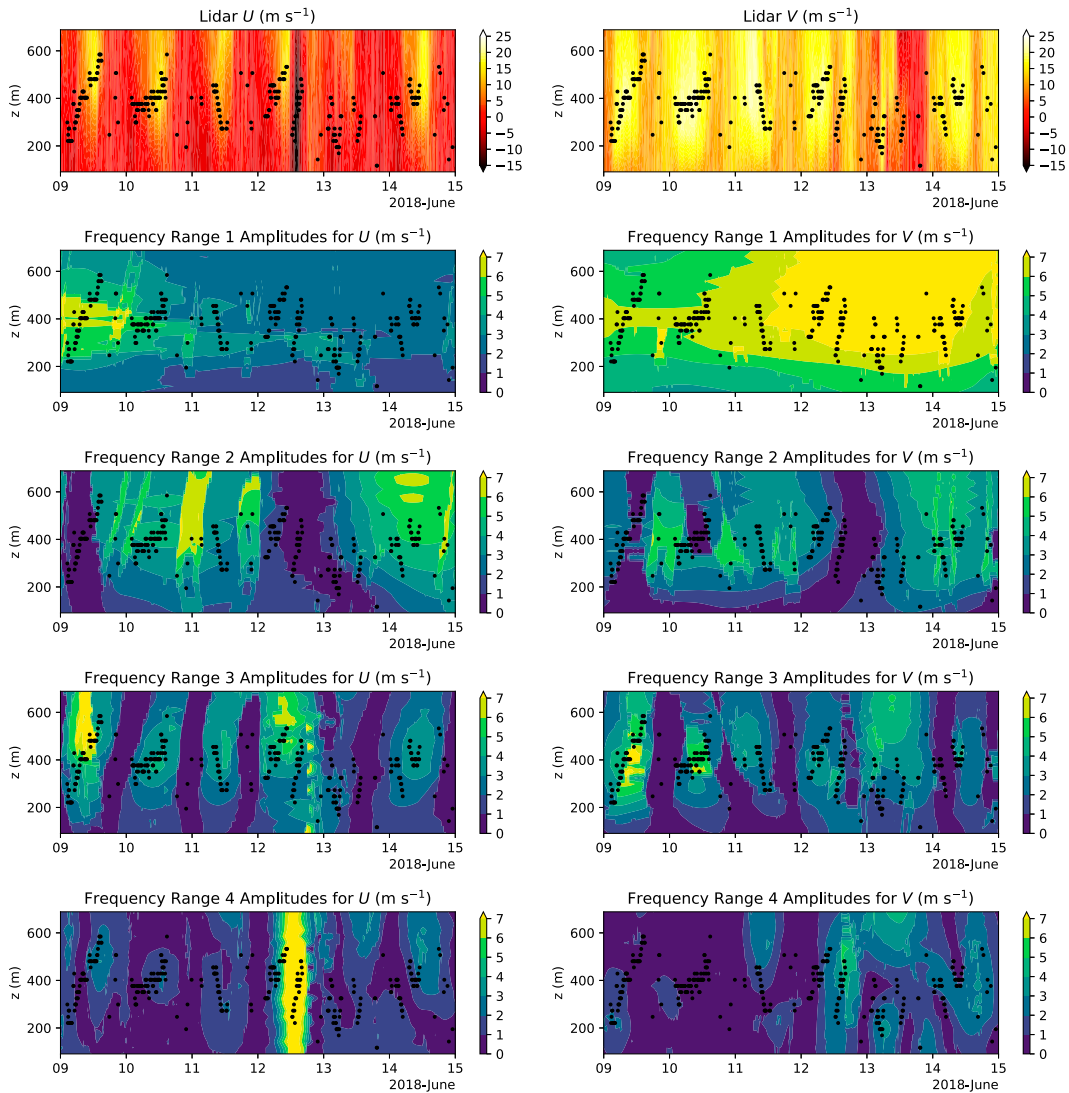


FIG. 8. Instantaneous HHT amplitudes (units: m s^{-1}), summed over IMFs, in four frequency ranges (see Table 1) of U and V velocity components for lidar data from the SGP ARM site C1 from 9 to 15 Jun 2018. The time and jet-set height of each LLJ occurrence detected during this time period is marked with a black dot on all plots. Note the difference in scales of altitude vs Figs. 9–11 due to the larger vertical extent of the ARM lidar data availability relative to the NYSERDA dataset.

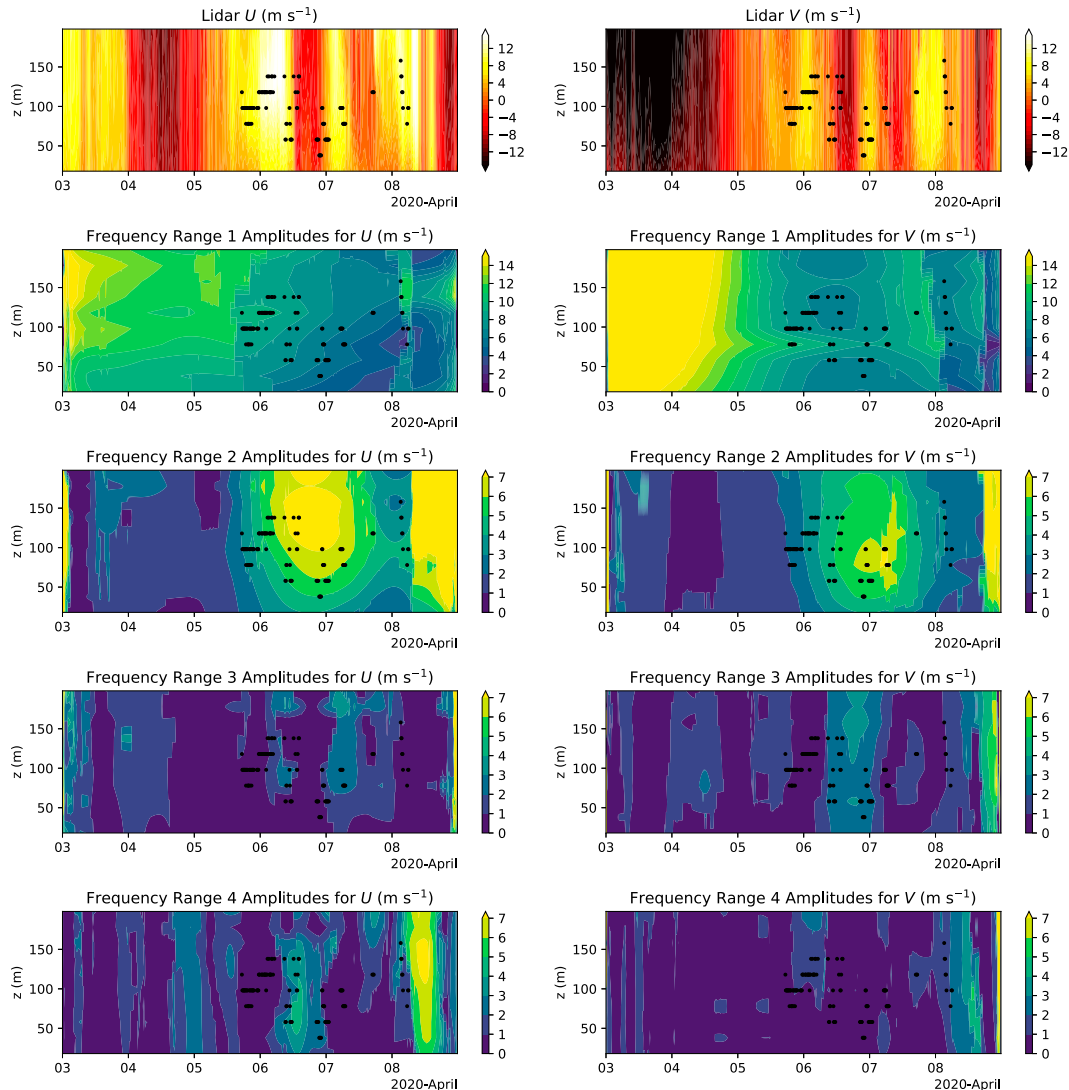


FIG. 9. Instantaneous HHT amplitudes (units: m s^{-1}), summed over IMFs, in four frequency ranges (see Table 1) of (left) U and (right) V velocity components for lidar data from the E06 NYSERDA buoy on 3–8 Apr 2020. The time and jet-nose height of each LLJ occurrence detected during this time period is marked with a black dot on all plots.

range 2 and a subinertial frequency range 3 that is distinct from mesoscale motions (range 4). As noted in Zhang et al. (2006), a horizontally sheared environment will exhibit a modified inertial frequency, which may explain inertial mechanisms manifesting in the diurnal or subinertial frequency range. Altogether, the frequency ranges investigated (Table 1) are inclusive of all frequencies spanning slow synoptic scales of 1×10^{-6} Hz (type 1) to faster mesoscales of 5×10^{-5} Hz.

To further distinguish the relative roles of each characteristic frequency in the overall wind velocity signals, we consider the amplitudes associated with each frequency type locally in altitude and height in Figs. 8–11. Amplitudes are reported in units of meters per second, following the HHT procedure, and generally decrease as the frequency of the associated

HHT increases, as seen in Fig. 7. The color bars in Figs. 9–11 are rescaled accordingly to depict local variations in the HHT amplitudes. These amplitudes indicate the energy associated with mechanisms at the associated range of time scales and can be used to identify the contribution of different physical processes to the wind profiles (Helmis et al. 2015). For instance, synoptic-scale motions such as pressure systems and large-scale horizontal gradients exhibit strong signals in the lowest frequency range 1, evolving on the time scale of order 100 h (Helmis et al. 2015; Lundquist 2003). Medium-frequency motions corresponding to ranges 2 or 3 correspond to inertial or diurnal time scales, which would indicate an inertial oscillation or nocturnal forcing (Lundquist 2003; Helmis et al. 2013). Higher-frequency motions (range 4) are most representative

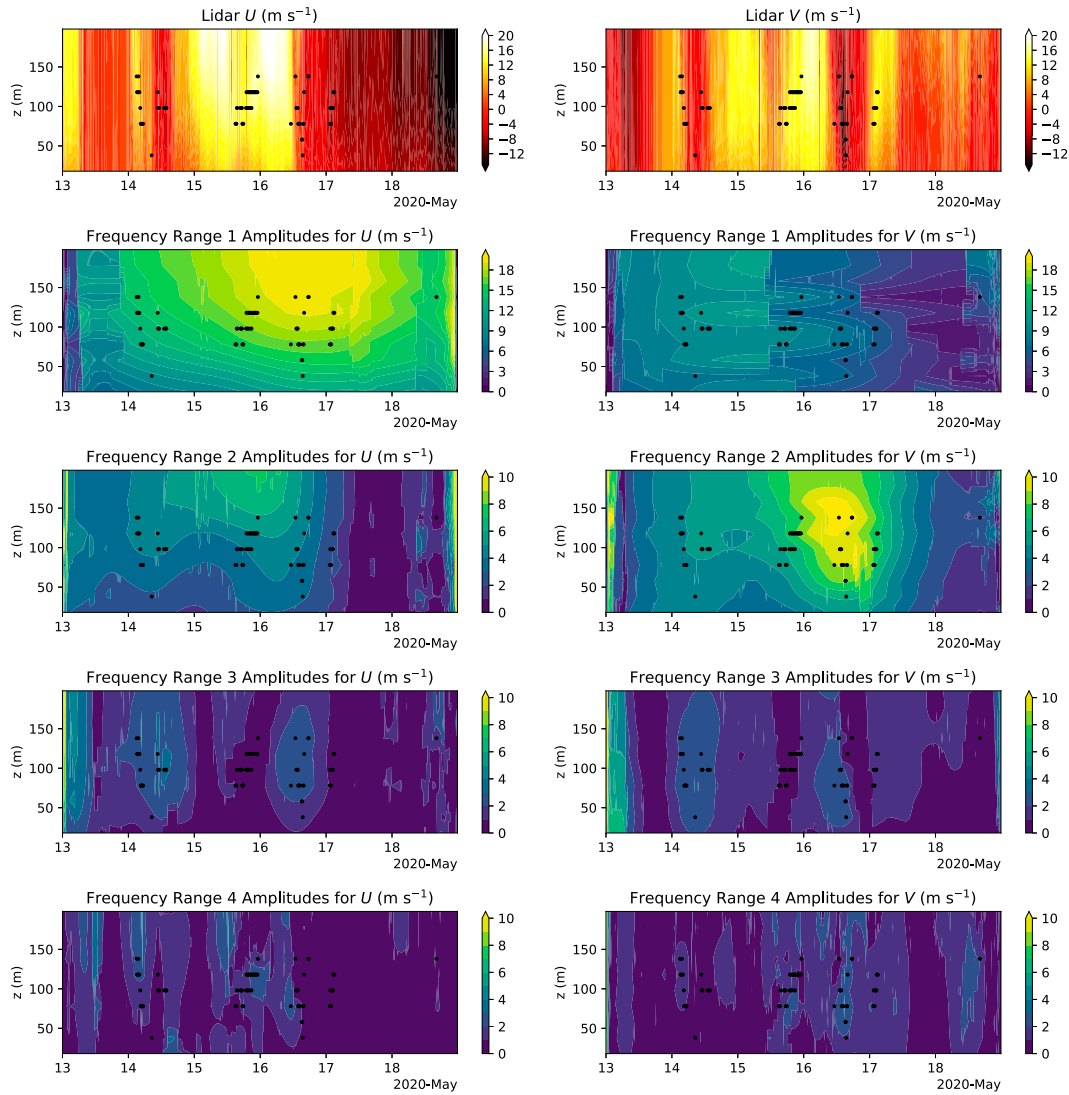


FIG. 10. As in Fig. 9, but for the date range 13–18 May 2020.

of mesoscale phenomena such as density currents, turbulence, or precipitation events. Fronts were referenced in Lundquist (2003) as both synoptic- and mesoscale phenomena, with a synoptic signature corresponding to the large-scale pressure gradients on either side of the front, and a mesoscale frequency of motion peaking when the barrier between the two air masses passes over the point of interest.

Beginning with the SGP datasets, we observe a clear cyclic pattern in the winds (Fig. 8, top row), with LLJs forming in the late evening local time (UTC – 5 h), and with the jet nose increasing in altitude and wind speeds intensifying through the morning until the jet dissipates. The amplitude contours for the U component indicate initial atmospheric motions in frequency range 1 around altitudes of 400 m. These motions dissipate throughout 10 June 2018, with a simultaneous increase in activity in frequency range 1 for the V component. Changes to this low-frequency signal are likely related to the

weakening of an initial east–west pressure gradient, followed by invasion of several pressure systems on subsequent days, but seem to have little correspondence with the presence of LLJs. Frequency types 2 and 3, however, are strongly anticorrelated and correlated, respectively, with LLJs. The diurnal frequency range (type 2) shows peak amplitudes during afternoon and daytime of the first four days of data, when incoming radiation has the strongest local impact on winds. Type 3 frequency signals are strongly in phase with the nocturnal LLJs. Furthermore, the 19-h period associated with these frequencies is sufficiently close to the 20-h inertial period, leading us to conclude that this signal provides evidence of an IO that drives LLJs in this dataset. Higher-frequency mesoscale signals (type 4) do not show a strong correspondence with LLJs but appear to be most related to smaller-scale fluctuations in velocity related to a high-precipitation event on 12 June 2018 (Bodini et al. 2021).

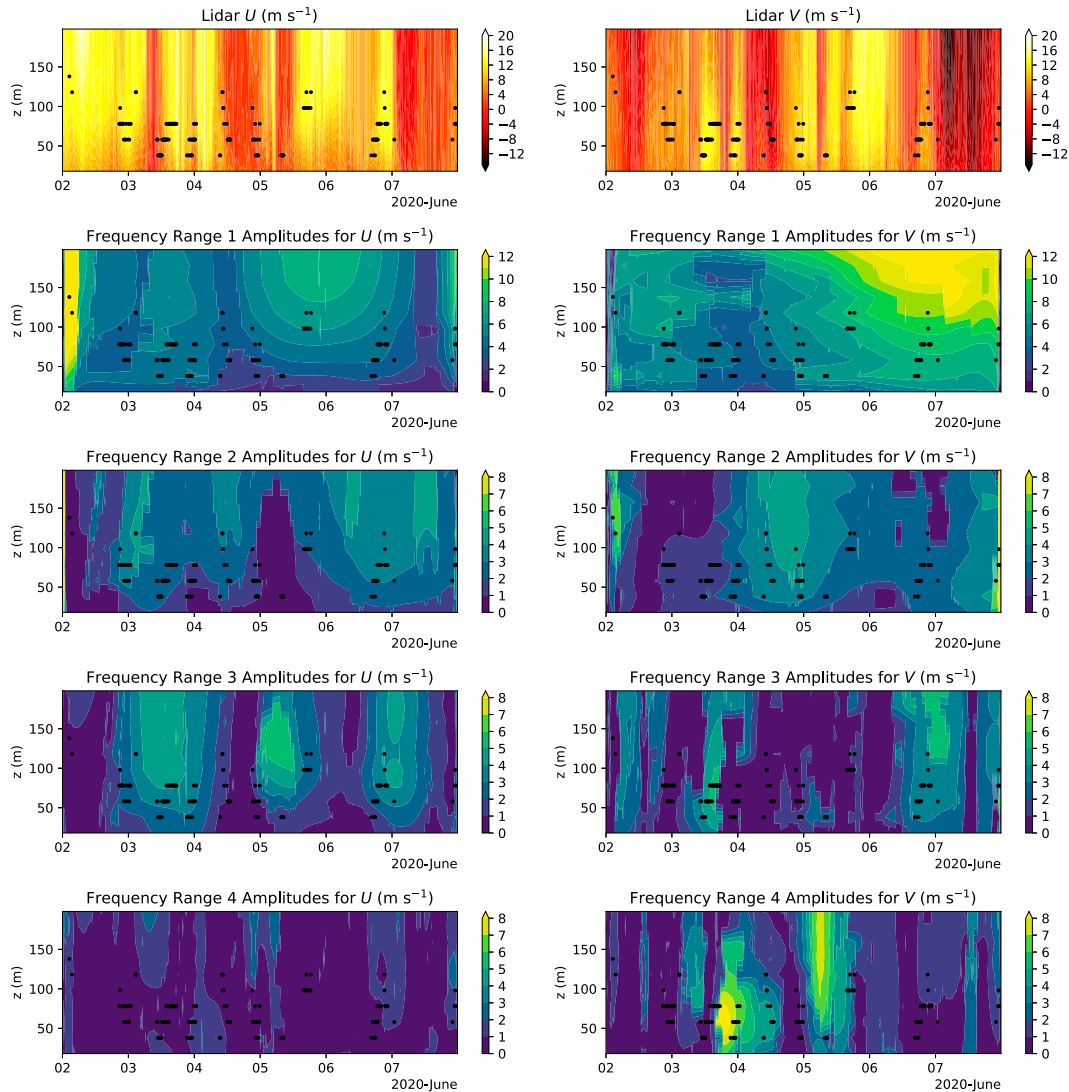


FIG. 11. As in Fig. 9, but for the date range 2–8 Jun 2020.

Analysis of the local-in-time HHT signal in the SGP demonstrates that this approach can distinguish known mechanisms of LLJs in the region, including synoptic-scale pressure gradient forcing, the diurnal cycle, and IOs. We therefore proceed to apply this analysis to the three case studies of springtime mid-Atlantic LLJs. Figure 9 reveals that the 3 April 2020 test case is characterized by initially strong synoptic (type 1) frequencies, which decrease in amplitude leading up to the initiation of a persistent LLJ in the evening of 5 April 2020. Note the color-bar scale of the type 1 amplitudes differs from types 2–4 as the associated amplitudes are much stronger in the springtime LLJ cases. Simultaneously, the amplitude of the type 2 signals, which contain the 22- and 27-h peaks noted in Fig. 7, pick up and are strongest at altitudes near the jet-nose height. The type 3 amplitudes show some diurnal variability and increase in both components during the LLJ event, and type 4 amplitudes show little correspondence with the jet event. The pattern seen on 5 April

reveals a downscaling of atmospheric motions: synoptic frequencies leading up to passage of a cold front on 6 April propagate diurnal or inertial frequency motions during the LLJ event, which persists through 7 April. Mesoscale frequencies are strongest in the V component during frontal passages on 6 and 9 April.

For the persistent jet on 15 May 2020, we observe a similar downscaling pattern in the V component of wind (Fig. 10), in which synoptic frequencies with amplitudes on the order of 10 m s^{-1} intensify ahead of a warm front moving from south to north on 15 May. These synoptic frequencies give way to type 2 frequencies at similar amplitudes during the jet event, particularly in the V component. The U component displays an increasing amplitude of type 1 synoptic frequencies during the LLJ event, particularly at the upper measurement altitude of 200 m, which is indicative of larger-scale pressure systems in the region. Neither the type 3 or 4 frequency appears to be

strongly correlated with the presence of a jet on this case date.

The 2–8 June 2020 case date manifests several intermittent LLJs with lower jet-nose heights than the 15 May or 5 April LLJs (Fig. 11). Frequency analysis of this June case does not display a coherent downscaling pattern from synoptic frequencies to higher-frequency motions, reflecting a relatively stationary high pressure system over the ocean southeast of the buoys and a lack of frontal motions until a southeast-moving cold front forms on 6 June, passing the buoy on 7 June. (A signature of this cold front is seen in increasing type 1 amplitudes in the U velocity component.) None of the frequency ranges show consistent amplitude increases that coincide with the presence of intermittent LLJs on 3–7 June. However, three spikes in lower-frequency (type 3) signals in the U component of velocity span a majority of the observed jet events, and a nonzero amplitude in the type 2 range is generally present throughout the time period. These characteristics indicate that this 6-day period is driven less by large-scale gradients in temperature and pressure or frontal systems, and more so by persistent pressure systems and motions at a near-diurnal/inertial frequency.

A similar frequency analysis of nonspringtime LLJ events at buoy E06 (plots not included) reveals significant amplitudes and variation in frequency range 1 and minimal signals in frequency ranges 2–4 around the time of jet occurrences. The air–sea temperature difference offers additional insight, as a positive difference supports a more stable boundary layer and favorable conditions for IO in springtime, and less favorable conditions at other times of year. As such, weaker signals in the inertial range may suggest that outside of the spring, the air–sea temperature difference is less crucial to the formation of jets.

These frequency analyses provide mounting evidence that IOs may play a role in driving springtime mid-Atlantic LLJs but not according to a nocturnal cycle of surface frictional decoupling. The presence of strong synoptic frequency motions that either dissipate just before LLJ events (5 April and 15 May) or coincide with the end of repeated LLJ events (7 June 2020) indicates that large-scale gradients are a key factor in these offshore jets. This finding corroborates the notion that LLJs are associated with frontal passages and points toward a baroclinic mechanism in which horizontal temperature gradients may drive a stationary LLJ in the thermal wind balance. Furthermore, evidence of inertial frequency motions that coincide with these springtime jets suggests that IOs may amplify a baroclinically driven jet through inertial acceleration.

c. Theoretical models

1) INERTIAL OSCILLATION

Fitting the wind velocity data from identified LLJ events to a model of IO [as in the conceptual model of Van de Wiel et al. (2010)] facilitates a better understanding of the contribution of IO to the jet. Hodographs at a single altitude in Fig. 12 illustrate the turning of the wind in the 5 April 2020 jet over an 18-h period. Fits to an IO are provided at the intrinsic inertial period of about 19 h, as well as a longer IO period of 22 h as identified by the peak in Fig. 7. Neither fit provides a clean

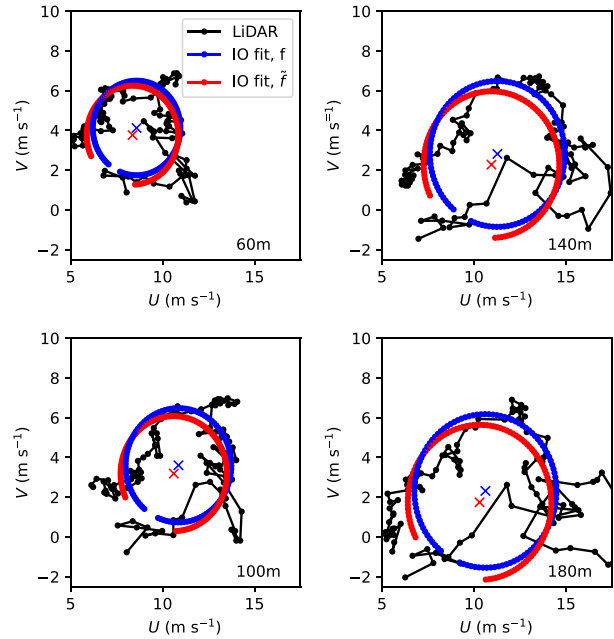


FIG. 12. Hodographs of NYSERDA buoy E06 wind data from 1700 UTC 5 Apr to 1100 UTC 6 Apr 2020 at four altitudes (labeled), with IO fits using a Coriolis parameter of $f = 9.31 \times 10^{-5} \text{ rad s}^{-1}$ (inertial period of 18.7 h) based on buoy latitude, and a modified inertial frequency of $\tilde{f} = 7.93 \times 10^{-5} \text{ rad s}^{-1}$ based on the finding of a 22-h period in the HHT spectra.

match to the absolute wind velocities, which fluctuate strongly in the later hours of the data, but the winds do show evidence of clockwise rotation with a time scale characteristic of IO.

Parameters of the IO fit [Eqs. (1)–(4)] are shown in Fig. 13 for all three springtime 2020 LLJ case studies previously discussed. The amplitude of the oscillation for the 5 April 2020 case is approximately double the root-mean-square (RMS) error in the IO fit, indicating that this simple model explains the wind speeds well during this event, while the 15 May 2020 case shows an RMS error profile of similar magnitude to the amplitude fit. These two cases indicate only marginal differences in the fitting parameters and RMS error when using the native versus modified inertial frequency, with a small reduction in error for the 5 April 2020 case at low altitudes. Notably, however, the steady-state velocity profiles of both cases display a local maximum in wind speed, indicating that the LLJ is a stationary phenomenon not dependent on inertial acceleration. This finding supports the idea of a thermal wind-driven jet, as in the baroclinic mechanism of Parish (2000), which is further enhanced by IOs.

Fitting the 4 June 2020 LLJ to an IO tells a different story. In this case, using a modified inertial period of 27 h dramatically improves the IO fit, as seen by the RMS error (Fig. 13, bottom right). The modified fit includes increased the magnitude of both steady-state wind components and the amplitude of the oscillation. A less obvious jet in the steady-state winds arises from the decreasing magnitude of v_{ss} with altitude as u_{ss} increases; the associated wind speeds of this steady state,

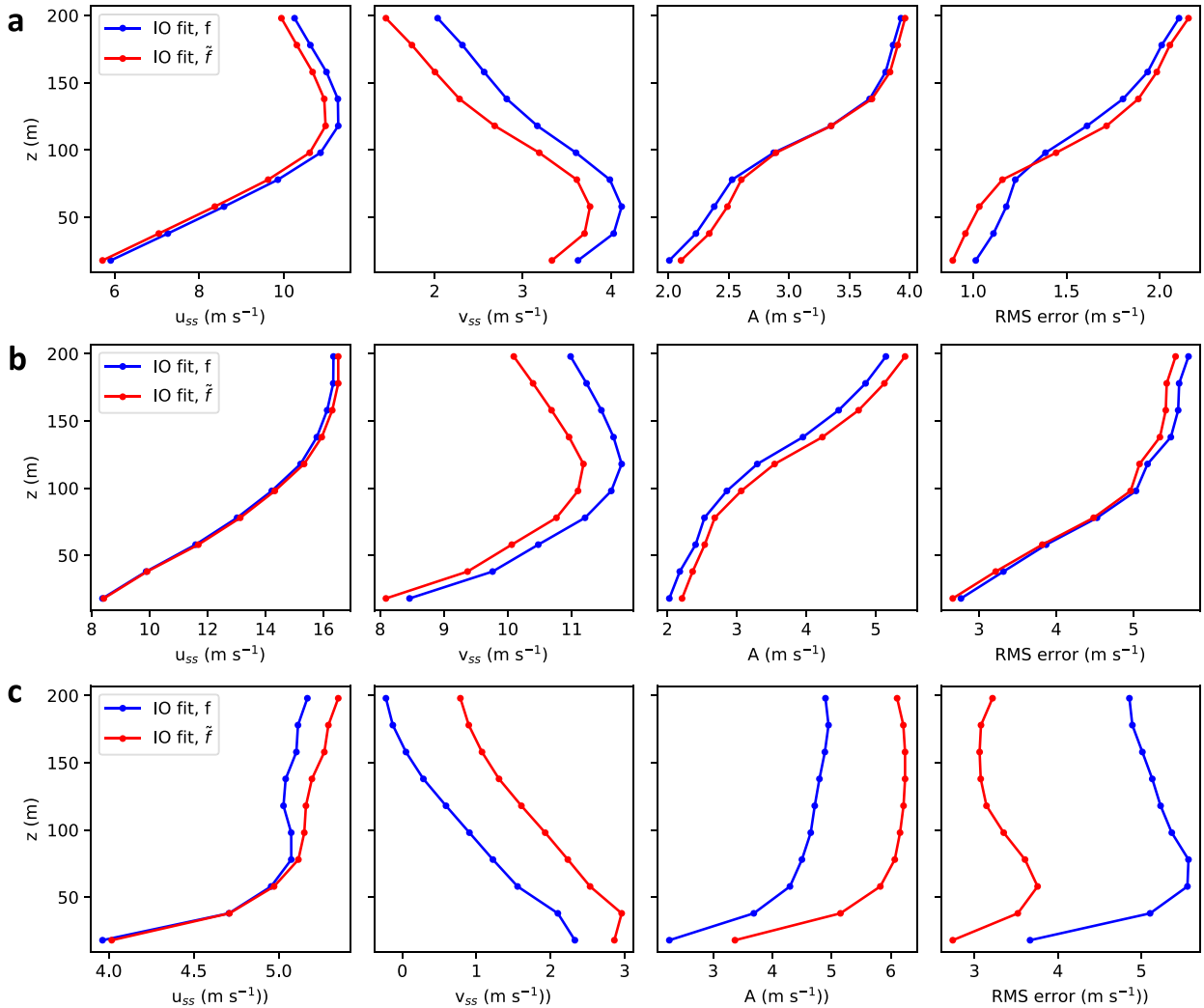


FIG. 13. (left to center right) Parameters of the IO fit using two different inertial frequencies, and (far right) the RMS error between the instantaneous fit velocities and measured velocities as a function of altitude. Fits are performed for (top to bottom) (a) 1700 UTC 5 Apr–1100 UTC 6 Apr 2020, (b) 1500 UTC 15 May–0900 UTC 16 May 2020, and (c) 0000 UTC 4 Jun–0000 UTC 5 Jun 2020. The modified Coriolis parameters \tilde{f} for the three cases were (a) 7.93×10^{-5} , (b) 7.93×10^{-5} , and (c) 6.46×10^{-5} rad s^{-1} compared to $f = 9.31 \times 10^{-5}$ rad s^{-1} .

however, are much lower than in the 5 April or 15 May jets, and are similar in magnitude to the amplitude A .

As noted by Zhang et al. (2006), the frequency of an IO in Blackadar's theory is modified to first order by horizontal shear as

$$\tilde{f} = \sqrt{f[f + \text{curl}(\mathbf{U}_g)]}, \quad (5)$$

where $\text{curl}(\mathbf{U}_g)$ is the curl of the geostrophic wind vector, corresponding to the horizontal shear. This modified inertial frequency may be greater or less than the native inertial frequency. (A derivation of this result is included in appendix B.) The difference in wind velocities between buoys E05 and E06 during the 15 May 2020 LLJ yields an estimated curl (or mean

shear) of -3.3×10^{-5} s^{-1} , which would modify the inertial period to 23 h, near the 22-h peak in Fig. 10. For the 5 April 2020 LLJ, the mean shear of 4.4×10^{-5} s^{-1} would decrease the inertial period to 15 h, corresponding to the smaller 14-h peak in the V component rather than the dominant observed 22-h peak. The 4 June 2020 LLJ experienced the most fitting improvement from using a modified horizontal shear. To modify this inertial frequency from 9.31×10^{-5} to 6.46×10^{-5} rad s^{-1} (period of 18.7–27 h) would require a horizontal shear of -2.0×10^{-5} s^{-1} . The estimated curl over the full 6-day period is -2.2×10^{-5} s^{-1} , which is in very good accord in both magnitude and sign. This observed horizontal shear indicates that the 27-h period is in fact characteristic of an inertial signal, which explains the improvement in fit to an IO model using this modified frequency.

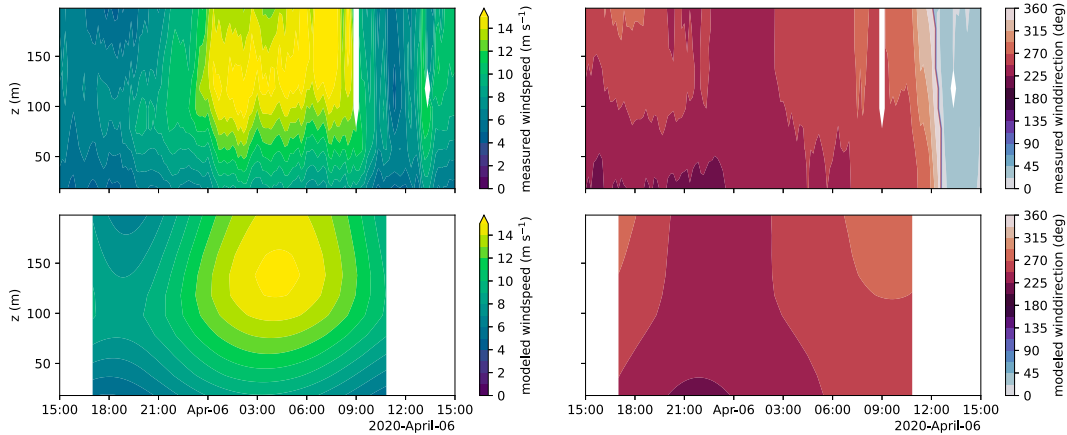


FIG. 14. (top) Measured wind speed and direction during 5 Apr 2020 LLJ at NYSERDA buoy E06 and (bottom) predicted winds from the IO fit with $f = 9.31 \times 10^{-5} \text{ rad s}^{-1}$ based on buoy latitude.

Figures 14–16 compare the observed and modeled wind speeds and directions for the same three LLJ events. In the case of 5 April and 15 May, the IO model captures the timing and magnitude of the local wind speed maximum, which rises in altitude and increases in strength before subsiding again. The IO model likewise does well in capturing the more subtle wind direction changes over the course of the two events but misses some of the vertical structure of wind-direction variation seen on 5 April 2020. For the repeated jets from 3 to 6 June 2020, Fig. 16 includes the IO model fit extended outside of the 27-h period of data used to fit the parameters. On 4 June 2020, the IO model predicts the wind direction structure and evolution of the LLJ extremely well, including the decreasing wind speeds that end the event around 1200 UTC. We find that extending this 27-h IO fit before and after the 4 June 2020 LLJ does not adequately explain the timing or magnitude of other recurring jets in this time period. The lack of predictability for these recurring jets points to additional mechanisms such as variations in the horizontal shear, which modify the inertial period, leading to deviations from a standard cyclic

nocturnal jet. Indeed, the horizontal shear from 2 to 3 June 2020 has an opposite sign from the mean at $3.6 \times 10^{-5} \text{ s}^{-1}$. This shear would result in a shortened inertial period of 15.9 h, and could correspond to the 14–15-h peak seen in Fig. 7.

2) THERMAL WIND

As in the work of Ostdiek and Blumen (1997), Fig. 17 demonstrates that the vertical structure of the steady-state wind profiles found in the IO model can be explained through an Ekman–Taylor balance. The freely varying fit to Eq. (4) allows the vertical gradients in U_g and V_g to vary during the optimization problem, while the constrained fit fixes these values based on estimated horizontal temperature gradients from a concurrent WRF run at the buoy site. Parameters of both fits are found in Table 2 (free) and Table 3 (constrained). Where applicable the fit parameters are related back to physical quantities: the Ekman depth H is related to the eddy viscosity as $H = (2\kappa/f)^{1/2}$, and the vertical gradients in geostrophic velocity are related to potential temperature θ via a thermal wind balance as

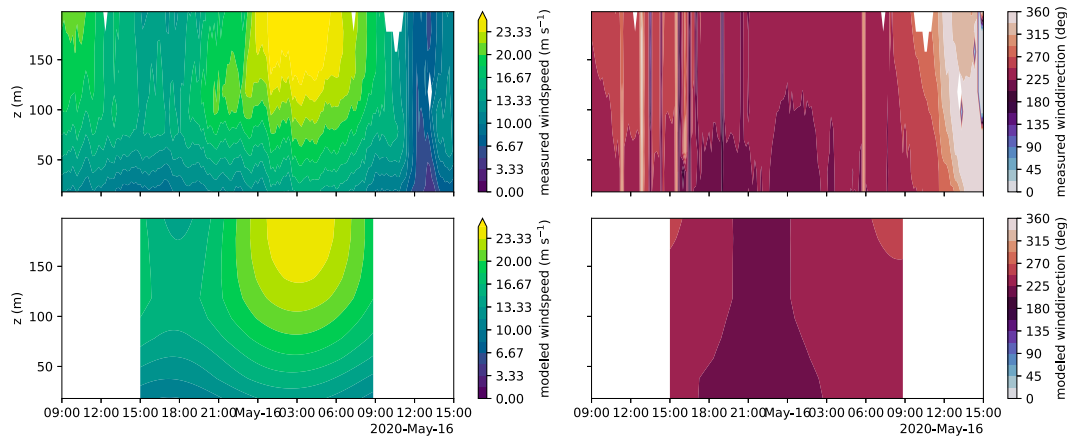


FIG. 15. (top) Measured wind speed and direction during 15 May 2020 LLJ at NYSERDA buoy E06, and (bottom) predicted winds from the IO fit with $f = 9.31 \times 10^{-5} \text{ rad s}^{-1}$ based on buoy latitude.

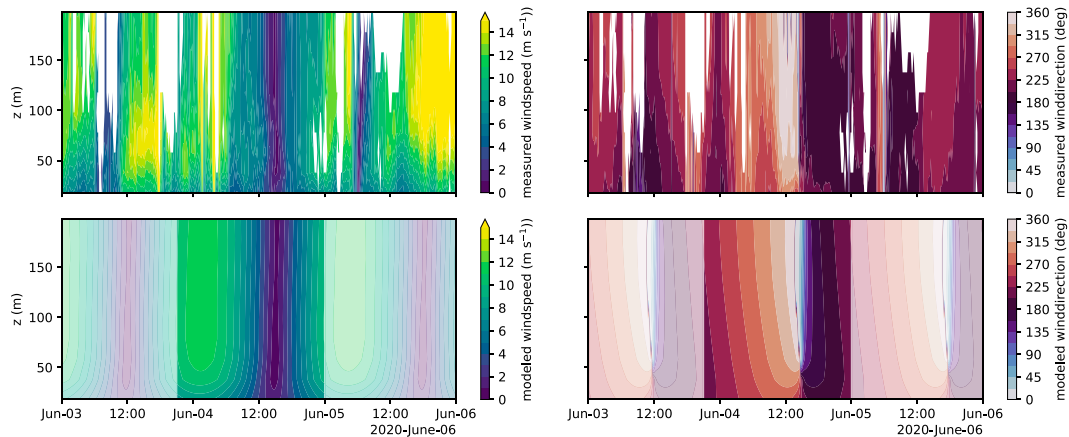


FIG. 16. (top) Measured wind speed and direction at NYSEERDA buoy E06, and (bottom) predicted winds from the IO fit with modified inertial frequency $\tilde{f} = 6.46 \times 10^{-5} \text{ rad s}^{-1}$ based on observed frequency spectra. Time periods that are not considered in fitting the IO parameters are grayed out but included for reference.

$U_{gz} = -(g/f\theta_0)(\partial\theta/\partial y)$ and $V_{gz} = (g/f\theta_0)(\partial\theta/\partial x)$. For the case of estimated temperature gradients, the implied geostrophic velocity gradients are estimated as $U_{gz} = -(g/fT_0)(\partial T/\partial y)$ (likewise for V_{gz}), where T_0 is the mean ambient air temperature.

The freely varying and the constrained version of these fits can reproduce the local maximum in winds for the 5 April and 15 May 2020 case dates, while the 4 June 2020 case is not well captured by the constrained fit (Fig. 17). The first two parameters A and H generally fall within a physical range for offshore conditions for 5 April and 15 May 2020 in both fits (Bannon and Salem 1995), interpreting H as proportional to the marine boundary layer height. The Ekman layer thickness for the 4 June 2020 case is particularly small, implying negligible vertical mixing. The eddy viscosity implied by the fitted H agrees with the finding of $A = 0.4$ (0.7 in the constrained case) for a nearly stress-free boundary (Bannon and Salem 1995), but both quantities are likely unreliable due to the worse fit of the IO model to this case. In the freely varying fit, the vertical gradients in geostrophic velocity imply potential temperature gradients on a realistic order of magnitude. However, the sign of the implied $\partial T/\partial x$ is counterintuitive. On 5 April and 15 May, the fits in Table 2 imply increasing potential temperatures to the north, consistent with estimates used in the constrained fit and physically consistent with land–sea temperature differences between the NY Bight and urban areas to the north, as noted by Colle and Novak (2010). However, the positive value of $\partial T/\partial x$ contradicts the expected land–sea temperature gradient as well as the estimated temperature gradients from WRF. Using these estimated gradients to derive the geostrophic velocity gradients, however, does not significantly impact the ability of the Ekman–Taylor model to fit the steady-state data for these two case dates. The north–south gradient in y is typically larger than the x gradient; thus, the consistency in sign of this quantity across the two fits helps to preserve the behavior of the model. Temperature gradients derived for 4 June generally agree in sign, but the constrained fit performs poorly by comparison.

However, the jet-nose maximum in the steady-state profile for this June case is much less pronounced, and the surrounding 6-day period experiences recurring LLJs. These factors indicate that the 4 June 2020 LLJ is driven more strongly by IO and frictional decoupling than by the baroclinic mechanism.

d. Limitations

Chief among the limitations of this work are the limited horizontal and vertical extent of the observational data, which restricts analysis to only two locations in the mid-Atlantic offshore, at altitudes of 200 m or lower. The vertical extent limits characterization of jets that may occur higher in the troposphere (e.g., Zhang et al. 2006; Colle and Novak 2010), but is sufficient to yield insights on very low LLJs, which are extremely relevant to wind energy. The criteria used to identify low-level jets (Debnath et al. 2021) are likewise specific to wind speed maxima that are most relevant to wind energy, and therefore, this study may underrepresent mechanisms that are responsible for additional classes of low-level jets. The two NYSEERDA buoys each yield only a single pressure and temperature measurement near the sea surface, which creates significant uncertainty in assessing atmospheric stability or horizontal gradients at altitudes outside of the surface layer. These challenges make it impossible to assess the absolute accuracy of the parameters found from thermal wind balance analysis or the power of this analysis as a predictive tool for LLJs. Finally, using only data from the two buoys does not allow us to draw conclusions about the regional or mesoscale extent of the LLJs under study.

Along the same lines, this work does not attempt to address the contribution of sloped terrain from Appalachia to these horizontal gradients, focusing instead on information that can be gleaned strictly from measurements over the NY Bight. Several of these uncertainties could be investigated using additional existing lidar buoys off the coast of New Jersey and Massachusetts, but a detailed analysis of all of these datasets is beyond the scope of this work. Reducing the uncertainties related to vertical resolution of the horizontal temperature

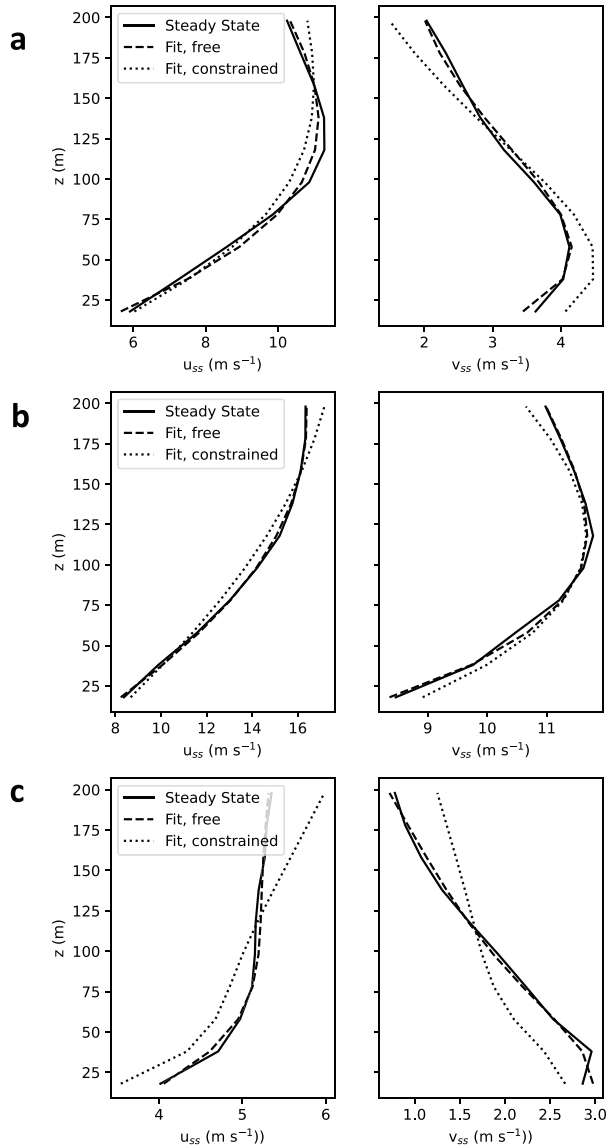


FIG. 17. Steady-state velocity profiles from IO fit (using inertial frequencies as in Figs. 14–16) vs Ekman–Taylor balance fit for (a) 5 Apr, (b) 15 May, and (c) 4 Jun 2020. Two version of the fit are shown: the freely varying fit, in which u_{gz} and v_{gz} are fit parameters, and the constrained fit, in which u_{gz} and v_{gz} are estimated from WRF Model output.

gradients in particular would require additional measurements beyond currently available data. Limitations in the temporal extent of the data, which only provide a 2-yr period of consistent readings at both buoys, also make it difficult to definitively characterize the statistical difference between jet and background events. This challenge is compounded by the gaps in data availability, such as the mentioned months-long gaps at E06. Atmospheric models could also provide missing information related to vertical and horizontal gradients in temperature and pressure, the mesoscale extent of the LLJ, and extend the date range of study, but previous studies using

weather models (e.g., Aird et al. 2022; Zhang et al. 2006) have shown that they struggle to consistently capture LLJ characteristics and are sensitive to parameterization choices (Rabenhorst et al. 2014). We therefore leave detailed analysis using weather model data to future work.

In addition, while this work describes an analytical model to explain the evolution of an LLJ due to horizontal temperature gradients and inertial oscillation, we do not attempt to model these gradients as a direct consequence of frontal activity or LSB, both of which are discussed as potential contributors. Further efforts to examine a larger geographic extent, higher-frequency statistics of frontal motions, and conceptual models of circulations induced by the fronts versus the LSB could elucidate the relative role and seasonality of these larger-scale factors, but they are beyond the scope of this work.

4. Conclusions

Analysis of LLJ events from the two NYSEDA buoys across a 2-yr period revealed that jets are predominantly southwesterly flows that occur in the springtime without a strong diurnal cycle, other than a dip in frequency during the nighttime. This lack of a diurnal cycle in jet occurrence separates these offshore mid-Atlantic LLJs from their SGP counterparts, pointing to mechanisms beyond IO. More specifically, the 2-yr statistics of the jets reveals a dominance of along-coast gradients in temperature and pressure, indicating that a baroclinic mechanism similar to that of the California coast (Parish 2000) drives mid-Atlantic jets. In this study, we focus on three case periods during spring 2020, two of which exhibited a frontal passage. Fronts are one example of such a large-scale gradient as seen by the statistically significant increase in LLJ event probability in the presence of a front. Land–sea breezes can play a dual role. By enhancing horizontal gradients, they contribute to the thermal wind balance mechanism. At the same time, the flow of warmer air over a cold sea during the springtime LSB contributes to atmospheric stability and conditions that favor IOs. HHT frequency analysis confirms this finding by revealing strong signals in synoptic-time-scale motions, as well as a downscaling of synoptic frequencies to modified inertial frequencies. Our analyses do not indicate a recurring diurnal signature, indicating that the LSB contributes to conditions of atmospheric stability for IOs to occur, rather than generating a sufficient horizontal gradient to trigger jets alone. Indeed, fitting data from specific LLJ events to conceptual models reveals that IO is an excellent match to the wind data but that a local maximum in wind speed occurs in the steady-state wind vector rather than resulting from the oscillation. This steady state can be explained by a thermal wind balance, further proving that large-scale temperature and pressure gradients are the dominant cause of LLJ formation and that inertial motions further modulate the timing and intensity of these jets.

Our findings build on existing studies of mid-Atlantic LLJs which focus on nocturnal jets (Zhang et al. 2006) or exclude synoptic-scale forcings (Rabenhorst et al. 2014) by providing a more general analysis of potential contributing factors

TABLE 2. Parameters of the freely varying Ekman–Taylor fits to steady-state winds from the IO model for three case dates and the physical quantities implied by these parameters. The eddy viscosity κ and gradients in θ (potential temperature) are computed using $f = 9.31 \times 10^{-5} \text{ rad s}^{-1}$, $g = 9.81 \text{ m}^2 \text{ s}^{-1}$, and $\theta_0 = 300 \text{ K}$.

Case	Fit parameters						Implied quantities		
	A	H (m)	U_{gz} (s^{-1})	V_{gz} (s^{-1})	U_{g0} (m s^{-1})	V_{g0} (m s^{-1})	κ ($\text{m}^2 \text{ s}^{-1}$)	$\partial\theta/\partial x$ (K km^{-1})	$\partial\theta/\partial y$ (K km^{-1})
5 Apr 2020	3.1	98	−0.022	0.012	13.6	−1.3	0.45	0.033	0.062
15 May 2020	2.5	155	−0.038	0.016	24.3	2.7	1.13	0.045	0.011
4 Jun 2020	0.4	40	0.002	−0.011	4.9	2.8	0.07	−0.030	−0.006

without presupposing or excluding potential mechanisms. However, the results and analyses in this study rely on only two observational stations and therefore require further corroboration to confirm the geographic extent of the mechanisms considered. For instance, the causes and characteristics of LLJs are likely to change with increased proximity to the coastline, where the land–sea breeze, warm surface temperatures, and/or topographic effects may contribute more strongly. Nevertheless, this research contributes to our understanding of mid-Atlantic jets by demonstrating that synoptic-scale gradients in temperature and pressure are a key feature for jets to form in the region. IOs, stemming from stability induced by the LSB, enhance LLJ behavior over an approximately stationary background flow. The dominance of the baroclinic mechanism suggests that correct prediction of frontal events and pressure systems is a key criterion for weather forecasting models to be useful predictive tools for LLJs. IOs during jet events are likely to be particularly important considerations for operation of future offshore wind plants due to their impacts on the peak wind speeds, altitude of the wind speed maximum, negative vertical wind shear, and directional shear, all of which have been shown to be important to wind-turbine operation and performance (Gutierrez et al. 2016, 2019; Zhang et al. 2019; Doosttalab et al. 2020; Gadde and Stevens 2021a,b; Chatterjee et al. 2022). These impacts may have implications for individual turbine control to reduce fatigue or wind plant control to maximize power production under LLJ conditions. Given the novelty of offshore wind development and deployment in the U.S. mid-Atlantic coastal offshore, this study may inform the design, deployment, and ultimate operation of offshore wind energy projects in the NY Bight and nearby lease areas.

Acknowledgments. E. de Jong acknowledges funding support from the U.S. Department of Energy Computational Sciences Graduate Fellowship. This material is based upon

work supported by the U.S. Department of Energy’s Office of Energy Efficiency and Renewable Energy (EERE) under the Wind Energy Technologies Office Award DE-EE0008390 to the New York State Energy Research and Development Authority for establishing the National Offshore Wind Research Consortium. This report was prepared as an account of work sponsored by an agency of the U.S. Government. Neither the U.S. Government nor any agency thereof, nor any of their employees, makes any warranty, express or implied, or assumes any legal liability or responsibility for the accuracy, completeness, or usefulness of any information, apparatus, product, or process disclosed, or represents that its use would not infringe privately owned rights. Reference herein to any specific commercial product, process, or service by trade name, trademark, manufacturer, or otherwise does not necessarily constitute or imply its endorsement, recommendation, or favoring by the U.S. Government or any agency thereof. The views and opinions of authors expressed herein do not necessarily state or reflect those of the U.S. Government or any agency thereof.

Data availability statement. All scripts used in data analysis and modeling are archived at <https://doi.org/10.5281/zenodo.8271338>. The NYSERDA floating lidar buoy data used in this study are publicly accessible online at <https://oswbuoysny.resourcepanorama.dnv.com/> (NYSERDA 2022). Doppler lidar data from the ARM SGP site C1 can likewise be downloaded from <https://www.arm.gov/data/data-sources> (Newsom and Krishnamurthy 2023). Surface analysis images used to identify fronts are available from the National Weather Service Weather Prediction Center archive at https://www.wpc.ncep.noaa.gov/archives/web_pages/sfc/sfc_archive.php. WRF data from the mid-Atlantic region are archived through the Open Energy Data Initiative at <https://data.openeye.org/submissions/4500> (Bodini et al. 2020).

TABLE 3. As in Table 2, but for the gradient-constrained Ekman–Taylor fits to steady-state winds from the IO model for three case dates and the physical quantities implied by these parameters.

Case	Physical parameters		Fit parameters				Implied quantities		
	$\partial T/\partial x$ (K km^{-1})	$\partial T/\partial y$ (K km^{-1})	A	H (m)	U_{g0} (m s^{-1})	V_{g0} (m s^{-1})	κ ($\text{m}^2 \text{ s}^{-1}$)	U_{gz} (s^{-1})	V_{gz} (s^{-1})
5 Apr 2020	−0.0135	0.0182	1.7	86	11.6	2.0	0.35	−0.006	−0.005
15 May 2020	−0.0231	0.0911	2.1	210	27.6	5.4	2.0	−0.033	−0.008
4 Jun 2020	−0.0145	−0.0282	0.7	25	4.0	2.3	0.03	0.010	−0.005

APPENDIX A

Reference Map

For reference, Fig. A1 shows the location of the two lidar buoys in reference to the location of an identified warm front on 15 May 2023. Also depicted is the 100-km radius used to identify fronts from the surface analysis archives; in this instance, a warm front is detected in the region.

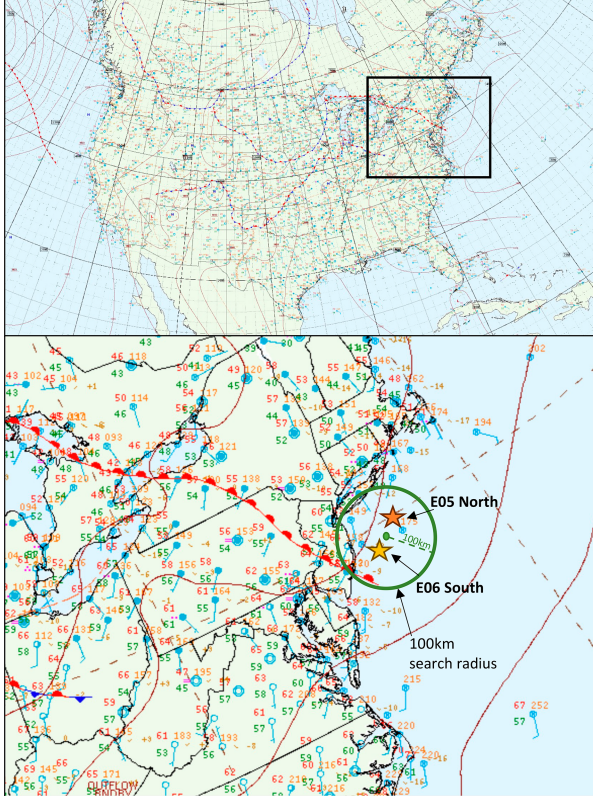


FIG. A1. (top) NOAA WPC detailed surface analysis map from 0900 UTC 15 May 2020 retrieved from <https://www.wpc.ncep.noaa.gov/html/sfc-zoom.php>, with the box depicting geographic extent of (bottom) a zoomed version of the same surface analysis overlaid with locations of the two lidar buoys and the 100-km search radius for fronts.

APPENDIX B

Derivation of the Horizontal Shear Modification

To begin, we assume zero vertical velocity and horizontal velocity components that can be decomposed into a stationary geostrophic component and a fluctuating component, $U_g(x, y, z)$ and $u'(z, t)$, respectively:

$$\begin{aligned} u &= U_g(x, y, z) + u'(z, t), \\ v &= V_g(x, y, z) + v'(z, t), \\ w &= 0. \end{aligned} \tag{B1}$$

We further assume that shear in the geostrophic components ($\partial U_g/\partial x$, $\partial U_g/\partial y$, $\partial V_g/\partial x$, and $\partial V_g/\partial y$) are constant or variable in z only.

The two-dimensional governing equations can be expressed as

$$\frac{\partial u}{\partial t} + u \frac{\partial U_g}{\partial x} + v \frac{\partial U_g}{\partial y} - f(v - V_g) = \kappa \nabla^2 u, \tag{B2}$$

$$\frac{\partial v}{\partial t} + u \frac{\partial V_g}{\partial x} + v \frac{\partial V_g}{\partial y} + f(u - U_g) = \kappa \nabla^2 v, \tag{B3}$$

where frictional terms have been reexpressed with the convention of an eddy viscosity κ . Applying the decomposed velocities from Eq. (B1), we find

$$\frac{\partial u'}{\partial t} = -(U_g + u') \frac{\partial U_g}{\partial x} - (V_g + v') \frac{\partial U_g}{\partial y} + f v' + \kappa \frac{\partial^2 (U_g + u')}{\partial z^2}, \tag{B4}$$

$$\frac{\partial v'}{\partial t} = -(U_g + u') \frac{\partial V_g}{\partial x} - (V_g + v') \frac{\partial V_g}{\partial y} - f u' + \kappa \frac{\partial^2 (V_g + v')}{\partial z^2}. \tag{B5}$$

With frictional decoupling, we assume that diffusion does not act on the time-varying fluctuations in the horizontal velocity. We can therefore write the governing equations as a state equation $(\partial/\partial t)\mathbf{u}' = \mathbf{A}\mathbf{u}' + \mathbf{F}$:

$$\frac{\partial u'}{\partial t} = \left(-\frac{\partial U_g}{\partial x}\right)u' + \left(-\frac{\partial U_g}{\partial y} + f\right)v' - U_g \frac{\partial U_g}{\partial x} - V_g \frac{\partial U_g}{\partial y} + \kappa \frac{\partial^2 U_g}{\partial z^2}, \tag{B6}$$

$$\frac{\partial v'}{\partial t} = \left(-\frac{\partial V_g}{\partial x} - f\right)u' + \left(-\frac{\partial V_g}{\partial y}\right)v' - U_g \frac{\partial V_g}{\partial x} - V_g \frac{\partial V_g}{\partial y} + \kappa \frac{\partial^2 V_g}{\partial z^2}. \tag{B7}$$

The eigenvalues of A determine the free response of the state equation. In a zeroth-order approximation, one can assume that the Coriolis parameter is much larger than horizontal shear, that is $U_y, V_x \ll f$, and thus, the eigenvalues are simply $\pm if$. (For simplicity, we abbreviate $\partial U_g/\partial x = U_x$ and likewise for gradients in y and for component V_g , where the subscript indicates “differentiation with respect to.”) For a higher-order approximation, we retain the horizontal shear to find eigenvalues λ of A :

$$\begin{aligned} \lambda &= -\frac{1}{2}(U_x + V_y) \\ &\pm \frac{1}{2}\sqrt{(U_x + V_y)^2 - 4[f^2 + (V_x - U_y)f + (U_x V_y - V_x U_y)]}. \end{aligned} \tag{B8}$$

Retaining terms that are linear in U_y and V_x and discarding quadratic and higher-order terms, the approximate eigenvalues for this damped harmonic oscillator then become

$$\begin{aligned}\lambda &= -\frac{1}{2}(U_x + V_y) \pm \sqrt{-f^2 - (V_x - U_y)f} \\ &= -\frac{1}{2}(U_x + V_y) \pm i\sqrt{f[f + (V_x - U_y)]}.\end{aligned}\quad (\text{B9})$$

The oscillating portion of the solution therefore has a modified inertial frequency:

$$\tilde{f} = \sqrt{f[f + (V_x - U_y)]}, \quad (\text{B10})$$

where the modification represents a curl in the geostrophic wind vector, $\text{curl}(\mathbf{U}_g) = (V_x - U_y)$, arising from horizontal shear.

REFERENCES

- Aird, J. A., R. J. Barthelmie, T. J. Shepherd, and S. C. Pryor, 2022: Occurrence of low-level jets over the eastern U.S. coastal zone at heights relevant to wind energy. *Energies*, **15**, 445, <https://doi.org/10.3390/en15020445>.
- Andreas, E. L., K. J. Claffy, and A. P. Makshtas, 2000: Low-level atmospheric jets and inversions over the western Weddell Sea. *Bound.-Layer Meteor.*, **97**, 459–486, <https://doi.org/10.1023/A:1002793831076>.
- Baas, P., F. C. Bosveld, H. K. Baltink, and A. A. M. Holtslag, 2009: A climatology of nocturnal low-level jets at Cabauw. *J. Appl. Meteor. Climatol.*, **48**, 1627–1642, <https://doi.org/10.1175/2009JAMC1965.1>.
- Bannon, P. R., and T. L. Salem Jr., 1995: Aspects of the baroclinic boundary layer. *J. Atmos. Sci.*, **52**, 574–596, [https://doi.org/10.1175/1520-0469\(1995\)052<0574:AOTBBL>2.0.CO;2](https://doi.org/10.1175/1520-0469(1995)052<0574:AOTBBL>2.0.CO;2).
- Beardsley, R. C., C. E. Dorman, C. A. Friehe, L. K. Rosenfeld, and C. D. Winant, 1987: Local atmospheric forcing during the Coastal Ocean Dynamics Experiment: 1. A description of the marine boundary layer and atmospheric conditions over a Northern California upwelling region. *J. Geophys. Res.*, **92**, 1467–1488, <https://doi.org/10.1029/JC092iC02p01467>.
- Blackadar, A. K., 1957: Boundary layer wind maxima and their significance for the growth of nocturnal inversions. *Bull. Amer. Meteor. Soc.*, **38**, 283–290, <https://doi.org/10.1175/1520-0477-38.5.283>.
- Bodini, N., M. Optis, M. Rossol, A. Rybchuk, and S. Redfern, 2020: US offshore wind resource data for 2000–2020. Open Energy Data Initiative, accessed 2 August 2023, <https://doi.org/10.25984/1821404>.
- , J. K. Lundquist, and P. Moriarty, 2021: Wind plants can impact long-term local atmospheric conditions. *Sci. Rep.*, **11**, 22939, <https://doi.org/10.1038/s41598-021-02089-2>.
- Burk, S. D., and W. T. Thompson, 1996: The summertime low-level jet and marine boundary layer structure along the California coast. *Mon. Wea. Rev.*, **124**, 668–686, [https://doi.org/10.1175/1520-0493\(1996\)124<0668:TSLJJA>2.0.CO;2](https://doi.org/10.1175/1520-0493(1996)124<0668:TSLJJA>2.0.CO;2).
- Carroll, B. J., B. B. Demoz, and R. Delgado, 2019: An overview of low-level jet winds and corresponding mixed layer depths during PECAN. *J. Geophys. Res. Atmos.*, **124**, 9141–9160, <https://doi.org/10.1029/2019JD030658>.
- Chatterjee, T., J. Li, S. Yellapantula, B. Jayaraman, and E. Quon, 2022: Wind farm response to mesoscale-driven coastal low level jets: A multiscale large eddy simulation study. *J. Phys. Conf. Ser.*, **2265**, 022004, <https://doi.org/10.1088/1742-6596/2265/2/022004>.
- Colle, B. A., and D. R. Novak, 2010: The New York Bight jet: Climatology and dynamical evolution. *Mon. Wea. Rev.*, **138**, 2385–2404, <https://doi.org/10.1175/2009MWR3231.1>.
- Cuxart, J., and M. A. Jiménez, 2007: Mixing processes in a nocturnal low-level jet: An LES study. *J. Atmos. Sci.*, **64**, 1666–1679, <https://doi.org/10.1175/JAS3903.1>.
- Debnath, M., P. Doubrawa, M. Optis, P. Hawbecker, and N. Bodini, 2021: Extreme wind shear events in US offshore wind energy areas and the role of induced stratification. *Wind Energy Sci.*, **6**, 1043–1059, <https://doi.org/10.5194/wes-6-1043-2021>.
- Delgado, R., S. D. Rabenhorst, B. B. Demoz, and R. M. Hoff, 2015: Elastic lidar measurements of summer nocturnal low level jet events over Baltimore, Maryland. *J. Atmos. Chem.*, **72**, 311–333, <https://doi.org/10.1007/s10874-013-9277-2>.
- Doosttalab, A., D. Siguenza-Alvarado, V. Pulletikurthi, Y. Jin, H. Bocanegra Evans, L. P. Chamorro, and L. Castillo, 2020: Interaction of low-level jets with wind turbines: On the basic mechanisms for enhanced performance. *J. Renewable Sustainable Energy*, **12**, 053301, <https://doi.org/10.1063/5.0017230>.
- Douglas, M. W., 1995: The summertime low-level jet over the Gulf of California. *Mon. Wea. Rev.*, **123**, 2334–2347, [https://doi.org/10.1175/1520-0493\(1995\)123<2334:TSLLJO>2.0.CO;2](https://doi.org/10.1175/1520-0493(1995)123<2334:TSLLJO>2.0.CO;2).
- Doyle, J. D., and T. T. Warner, 1991: A Carolina coastal low-level jet during GALE IOP 2. *Mon. Wea. Rev.*, **119**, 2414–2428, [https://doi.org/10.1175/1520-0493\(1991\)119<2414:ACCLLJ>2.0.CO;2](https://doi.org/10.1175/1520-0493(1991)119<2414:ACCLLJ>2.0.CO;2).
- Du, Y., and R. Rotunno, 2014: A simple analytical model of the nocturnal low-level jet over the Great Plains of the United States. *J. Atmos. Sci.*, **71**, 3674–3683, <https://doi.org/10.1175/JAS-D-14-0060.1>.
- Gadde, S. N., and R. J. A. M. Stevens, 2021a: Effect of low-level jet height on wind farm performance. *J. Renewable Sustainable Energy*, **13**, 013305, <https://doi.org/10.1063/5.0026232>.
- , and —, 2021b: Interaction between low-level jets and wind farms in a stable atmospheric boundary layer. *Phys. Rev. Fluids*, **6**, 014603, <https://doi.org/10.1103/PhysRevFluids.6.014603>.
- Gaertner, E., J. Rinker, L. Sethuraman, F. Zahle, B. Anderson, G. Barter, N. Abbass, and F. Meng, 2020: Definition of the IEA 15-megawatt offshore reference wind. NREL Tech. Rep. TP-5000-75698, 54 pp., <https://www.nrel.gov/docs/fy20osti/75698.pdf>.
- Gutierrez, W., G. Araya, P. Kiliyanpilakkil, A. Ruiz-Columbie, M. Tutkun, and L. Castillo, 2016: Structural impact assessment of low level jets over wind turbines. *J. Renewable Sustainable Energy*, **8**, 023308, <https://doi.org/10.1063/1.4945359>.
- , A. Ruiz-Columbie, M. Tutkun, and L. Castillo, 2017: Impacts of the low-level jet’s negative wind shear on the wind turbine. *Wind Energy Sci.*, **2**, 533–545, <https://doi.org/10.5194/wes-2-533-2017>.
- , —, —, and —, 2019: The structural response of a wind turbine under operating conditions with a low-level jet. *Renewable Sustainable Energy Rev.*, **108**, 380–391, <https://doi.org/10.1016/j.rser.2019.03.058>.
- Helmis, C. G., Q. Wang, G. Sgouros, S. Wang, and C. Halios, 2013: Investigating the summertime low-level jet over the East Coast of the U.S.A.: A case study. *Bound.-Layer Meteor.*, **149**, 259–276, <https://doi.org/10.1007/s10546-013-9841-y>.
- , G. Sgouros, and Q. Wang, 2015: On the vertical structure and spectral characteristics of the marine low-level jet. *Atmos. Res.*, **152**, 74–81, <https://doi.org/10.1016/j.atmosres.2013.11.005>.

- Higgins, R. W., Y. Yao, E. S. Yarosh, J. E. Janowiak, and K. C. Mo, 1997: Influence of the Great Plains low-level jet on summertime precipitation and moisture transport over the central United States. *J. Climate*, **10**, 418–507, [https://doi.org/10.1175/1520-0442\(1997\)010<0418:IOTGPL>2.0.CO;2](https://doi.org/10.1175/1520-0442(1997)010<0418:IOTGPL>2.0.CO;2).
- Högström, U., and A.-S. Smedman-Högström, 1984: The wind regime in coastal areas with special reference to results obtained from the Swedish wind energy program. *Bound.-Layer Meteor.*, **30**, 351–373, <https://doi.org/10.1007/BF00121961>.
- Holt, T. R., 1996: Mesoscale forcing of a boundary layer jet along the California coast. *J. Geophys. Res.*, **101**, 4235–4254, <https://doi.org/10.1029/95JD03231>.
- Holton, J. R., 1967: The diurnal boundary layer wind oscillation above sloping terrain. *Tellus*, **19A**, 199–205, <https://doi.org/10.3402/tellusa.v19i2.9766>.
- Kalashnik, M. V., 2004: Geostrophic adjustment and frontogenesis in a continuously stratified fluid. *Dyn. Atmos. Oceans*, **38**, 1–37, <https://doi.org/10.1016/j.dynatmoce.2004.01.001>.
- Lundquist, J. K., 2003: Intermittent and elliptical inertial oscillations in the atmospheric boundary layer. *J. Atmos. Sci.*, **60**, 2661–2673, [https://doi.org/10.1175/1520-0469\(2003\)060<2661:IAEIOI>2.0.CO;2](https://doi.org/10.1175/1520-0469(2003)060<2661:IAEIOI>2.0.CO;2).
- Maddox, R. A., 1983: Large-scale meteorological conditions associated with midlatitude, mesoscale convective complexes. *Mon. Wea. Rev.*, **111**, 1475–1493, [https://doi.org/10.1175/1520-0493\(1983\)111<1475:LSMCAW>2.0.CO;2](https://doi.org/10.1175/1520-0493(1983)111<1475:LSMCAW>2.0.CO;2).
- McCabe, E. J., and J. M. Freedman, 2023: Development of an objective methodology for identifying the sea-breeze circulation and associated low-level jet in the New York Bight. *Wea. Forecasting*, **38**, 571–589, <https://doi.org/10.1175/WAF-D-22-0119.1>.
- Mori, Y., 1990: Evidence of inertial oscillations of the surface wind at Marcus Island. *J. Geophys. Res.*, **95**, 11 777–11 783, <https://doi.org/10.1029/JD095iD08p11777>.
- Newsom, R., and R. Krishnamurthy, 2023: Doppler lidar (dlfpt). ARM User Facility, accessed 9 February 2023, <https://doi.org/10.5439/1025185>.
- NYSERDA, 2022: NYSERDA floating lidar buoy data. DNV, accessed 28 March 2023, <https://oswbuoysny.resourcepanorama.dnvgl.com/download/f67d14ad-07ab-4652-16d2-08d71f257da1>.
- Optis, M., O. Rybchuk, N. Bodini, M. Rossol, and W. Musial, 2020: 2020 offshore wind resource assessment for the California Pacific outer continental shelf. NREL Tech. Rep. NREL/TP-5000-77642, 61 pp., <https://doi.org/10.2172/1677466>.
- Ostdiek, V., and W. Blumen, 1995: Deformation frontogenesis: Observation and theory. *J. Atmos. Sci.*, **52**, 1487–1500, [https://doi.org/10.1175/1520-0469\(1995\)052<1487:DFOAT>2.0.CO;2](https://doi.org/10.1175/1520-0469(1995)052<1487:DFOAT>2.0.CO;2).
- , and —, 1997: A dynamic trio: Inertial oscillation, deformation frontogenesis, and the Ekman–Taylor boundary layer. *J. Atmos. Sci.*, **54**, 1490–1502, [https://doi.org/10.1175/1520-0469\(1997\)054<1490:ADTIOD>2.0.CO;2](https://doi.org/10.1175/1520-0469(1997)054<1490:ADTIOD>2.0.CO;2).
- Parish, T. R., 1982: Barrier winds along the Sierra Nevada mountains. *J. Appl. Meteor.*, **21**, 925–930, [https://doi.org/10.1175/1520-0450\(1982\)021<0925:BWATSN>2.0.CO;2](https://doi.org/10.1175/1520-0450(1982)021<0925:BWATSN>2.0.CO;2).
- , 1983: The influence of the Antarctic Peninsula on the wind field over the western Weddell Sea. *J. Geophys. Res.*, **88**, 2684–2692, <https://doi.org/10.1029/JC088iC04p02684>.
- , 2000: Forcing of the summertime low-level jet along the California coast. *J. Appl. Meteor.*, **39**, 2421–2433, [https://doi.org/10.1175/1520-0450\(2000\)039<2421:FOTSL>2.0.CO;2](https://doi.org/10.1175/1520-0450(2000)039<2421:FOTSL>2.0.CO;2).
- , and L. D. Oolman, 2010: On the role of sloping terrain in the forcing of the Great Plains low-level jet. *J. Atmos. Sci.*, **67**, 2690–2699, <https://doi.org/10.1175/2010JAS3368.1>.
- , A. R. Rodi, and R. D. Clark, 1988: A case study of the summertime Great Plains low level jet. *Mon. Wea. Rev.*, **116**, 94–105, [https://doi.org/10.1175/1520-0493\(1988\)116<0094:ACSOTS>2.0.CO;2](https://doi.org/10.1175/1520-0493(1988)116<0094:ACSOTS>2.0.CO;2).
- Quinn, A. J., V. Lopes-dos Santos, D. Dupret, A. C. Nobre, and M. W. Woolrich, 2021: EMD: Empirical mode decomposition and Hilbert-Huang spectral analyses in Python. *J. Open Source Software*, **6**, 2977, <https://doi.org/10.21105/joss.02977>.
- Rabenhorst, S., D. N. Whiteman, D.-L. Zhang, and B. Demoz, 2014: A case study of mid-Atlantic nocturnal boundary layer events during WAVES 2006. *J. Appl. Meteor. Climatol.*, **53**, 2627–2648, <https://doi.org/10.1175/JAMC-D-13-0350.1>.
- Ryan, W. F., and Coauthors, 1998: Pollutant transport during a regional O₃ episode in the mid-Atlantic states. *J. Air Waste Manage. Assoc.*, **48**, 786–797, <https://doi.org/10.1080/10473289.1998.10463737>.
- Sgouros, G., and C. G. Helmig, 2009: Low-level jet development and the interaction of different scale physical processes. *Meteor. Atmos. Phys.*, **104**, 213–228, <https://doi.org/10.1007/s00703-009-0028-5>.
- Shapiro, A., and E. Fedorovich, 2009: Nocturnal low-level jet over a shallow slope. *Acta Geophys.*, **57**, 950–980, <https://doi.org/10.2478/s11600-009-0026-5>.
- , and —, 2010: Analytical description of a nocturnal low-level jet. *Quart. J. Roy. Meteor. Soc.*, **136**, 1255–1262, <https://doi.org/10.1002/qj.628>.
- Shields, M., and Coauthors, 2022: The demand for a domestic offshore wind energy supply chain. NREL Tech. Rep. NREL/TP-5000-81602, 151 pp., <https://doi.org/10.2172/1860239>.
- Smedman, A.-S., M. Tjernström, and U. Högström, 1993: Analysis of the turbulence structure of a marine low-level jet. *Bound.-Layer Meteor.*, **66**, 105–126, <https://doi.org/10.1007/BF00705462>.
- , H. Bergström, and U. Högström, 1995: Spectra, variances and length scales in a marine stable boundary layer dominated by a low level jet. *Bound.-Layer Meteor.*, **76**, 211–232, <https://doi.org/10.1007/BF00709352>.
- U.S. Environmental Protection Agency, 2023: Summary of Inflation Reduction Act provisions related to renewable energy. EPA, <https://www.epa.gov/green-power-markets/summary-inflation-reduction-act-provisions-related-renewable-energy#:~:text=Through%20at%20least%202025%2C%20the,projects%20over%201%20MW%20AC>.
- Van de Wiel, B. J. H., A. F. Moene, G. J. Steeneveld, P. Baas, F. C. Bosveld, and A. A. M. Holtslag, 2010: A conceptual view on inertial oscillations and nocturnal low-level jets. *J. Atmos. Sci.*, **67**, 2679–2689, <https://doi.org/10.1175/2010JAS3289.1>.
- White House, 2021: Fact sheet: Biden Administration jumpstarts offshore wind energy projects to create jobs. White House Briefing Room, <https://www.whitehouse.gov/briefing-room/statements-releases/2021/03/29/fact-sheet-biden-administration-jumpstarts-offshore-wind-energy-projects-to-create-jobs/>.
- Wimhurst, J. J., and J. S. Greene, 2019: Oklahoma’s future wind energy resources and their relationship with the central plains low-level jet. *Renewable Sustainable Energy Rev.*, **115**, 109374, <https://doi.org/10.1016/j.rser.2019.109374>.
- Xia, G., C. Draxl, M. Optis, and S. Redfern, 2022: Detecting and characterizing simulated sea breezes over the US northeastern coast with implications for offshore wind energy. *Wind Energy Sci.*, **7**, 815–829, <https://doi.org/10.5194/wes-7-815-2022>.
- Zemba, J., and C. A. Friehe, 1987: The marine atmospheric boundary layer jet in the Coastal Ocean Dynamics

- Experiment. *J. Geophys. Res.*, **92**, 1489–1496, <https://doi.org/10.1029/JC092iC02p01489>.
- Zhang, D.-L., and J. M. Fritsch, 1986: Numerical simulation of the meso- β scale structure and evolution of the 1977 Johnstown flood. Part I: Model description and verification. *J. Atmos. Sci.*, **43**, 1913–1944, [https://doi.org/10.1175/1520-0469\(1986\)043<1913:NSOTMS>2.0.CO;2](https://doi.org/10.1175/1520-0469(1986)043<1913:NSOTMS>2.0.CO;2).
- , S. Zhang, and S. J. Weaver, 2006: Low-level jets over the mid-Atlantic states: Warm-season climatology and a case study. *J. Appl. Meteor. Climatol.*, **45**, 194–209, <https://doi.org/10.1175/JAM2313.1>.
- Zhang, X., C. Yang, and S. Li, 2019: Influence of the heights of low-level jets on power and aerodynamic loads of a horizontal axis wind turbine rotor. *Atmosphere*, **10**, 132, <https://doi.org/10.3390/atmos10030132>.